Combustion and Flame 267 (2024) 113538

Contents lists available at ScienceDirect

Combustion and Flame

journal homepage: www.sciencedirect.com/journal/combustion-and-flame

Combustion dynamics of ten-injector rocket engine using flamelet progress variable

Lei Zhan *, Tuan M. Nguyen[1], Juntao Xiong, Feng Liu, William A. Sirignano

Department of Mechanical and Aerospace Engineering, University of California, Irvine, CA 92697, USA

ARTICLE INFO

Keywords:
Combustion instability
Flamelet
Progress variable
Partially premixed flames
Turbulent combustion
Liquid rocket engine

ABSTRACT

Combustion instability is investigated computationally for a ten-injector rocket engine using a compressible flamelet progress variable (FPV) model and detached eddy simulation (DES). A C++ code is developed based on OpenFOAM 4.1 to apply the combustion model. Flamelet tables are generated for methane/oxygen combustion at the pressure of 200 bar using a 12-species chemical mechanism. The flames at this high pressure level have similar structures as those at much lower pressures. A power law is determined to rescale the reaction rate for the progress variable to address the pressure effect. The combustion is also simulated by a one-step-kinetics (OSK) model for comparison with the FPV model. Premixed and diffusion flames are identified locally for both the FPV and OSK models. Study of combustion instability shows that a combined first-longitudinal and first-tangential mode of 3200 Hz is dominant for the FPV model while the OSK model favors a pure first-tangential mode of 2600 Hz. The coupling among pressure oscillation, unsteady transverse flow and helicity fluctuation is discussed. A preliminary study of the resonance in the injectors, which is driven by the acoustic oscillation in the combustion chamber, is also presented.

Novelty and significance

In this paper, we demonstrate one of the first successful applications of a compressible flamelet-progress-variable (FPV) combustion model to numerical study of the methane/oxygen combustion dynamics and instability in a realistic multi-injector liquid rocket engine. A relatively detailed 12-species high-pressure chemical mechanism, which was originally developed by Professor Hai Wang's group at Stanford University, is applied for the first time to combustion simulation at chamber pressures around 200 bar. Compared with a one-step global kinetics model, the FPV model predicts realistic chamber temperature and favors a dominant combined 1L+1T acoustic mode at 3200 Hz rather than a pure 1T mode at 2600 Hz. The predicted dominant frequencies agree well with theoretical analysis. Strong quarter-wave-length resonance is found to occur inside injectors and coexist with the chamber acoustic oscillations.

1. Introduction

Combustion instability is an acoustical phenomenon in which an unstable pressure oscillation is excited and sustained by combustion. In most high-power propulsion systems for rockets and airplanes, the high-energy release rate reinforces high-amplitude acoustical oscillations. Such oscillations can affect thrust in an undesirable way and sometimes lead to engine destruction.

For more than a half century, it has been known that the relation between the characteristic time for combustion in liquid-propellant rocket engines and the resonant oscillation period is critical in determining the engine stability. Early pioneering work by Crocco and Cheng [1–3] established the principles using the sensitive time-lag concept in their analyses.

During the last two decades, there is an increasing need for three-dimensional high-fidelity numerical study of combustion instability in multi-injector rocket engines. Compared to the single-injector configuration, the combustion instability mechanism is more complex in a multi-injector combustion chamber because of the possible interactions among injectors and interactions with the complicated feed system and upstream manifold. Systematic experimental investigations of combustion instability for such configurations are quite expensive and technically difficult. Compared to experimental measurement, numerical simulations based on high-fidelity turbulence modeling and

* Corresponding author.
E-mail address: lzhan@uci.edu (L. Zhan).
[1] Current affiliation: Lawrence Livermore National Laboratory, Livermore, CA 94550, USA.

https://doi.org/10.1016/j.combustflame.2024.113538
Received 22 July 2023; Received in revised form 25 May 2024; Accepted 28 May 2024
Available online 15 June 2024

detailed chemical reaction mechanisms are able to provide more details about the flow physics as well as the combustion dynamics and hence allow us to gain a deeper insight into the combustion instability mechanisms. Among various instability modes, the transverse acoustic modes with large amplitude were observed in experiments under certain conditions [4–6]. Urbano et al. [7,8] carried out combustion simulations for a complete small-scale rocket engine with 42 coaxial injectors and a nozzle outlet. Large Eddy Simulations (LES) were employed and a four-species H_2/O_2 reacting mechanism was considered. Combustion instability was studied with emphasis on the interaction between transverse and radial modes. Under the experimental condition which leads to self-sustained oscillations, computational results showed that tangential instability can be triggered when the system is perturbed by superimposing a large-amplitude pressure disturbance with a first transverse modal distribution. Hwang et al. [9] employed their OpenFOAM-based code to study the combustion instability for the same multi-injector rocket engine. LES was also used while the combustion model was modified to consider a more detailed chemical mechanism with 8 species and 12 reaction steps. The same type of pressure perturbation was superimposed under the experimentally unstable condition and a pressure disturbance greater than a threshold value was needed to trigger the limit-cycle tangential oscillations. Guo et al. [10] investigated the transverse combustion instability of a 91-injector rocket engine using the standard Reynolds-Averaged Navier–Stokes (RANS) $k-\epsilon$ two-equation turbulence model and the eddy-dissipation combustion model. A single-step global chemical reaction mechanism was adopted to model the chemical reaction process of the Dodecane/oxygen combustion. Self-excited high-frequency combustion instability of first-order tangential (1T) mode was observed. Two different kinds of 1T patterns, standing wave mode and traveling wave mode, were captured for two different oxygen-to-fuel ratios.

Xiong et al. [11–13] presented computational studies of nonlinear rocket-engine combustion instability with 10-, 19-, 30-, and 82-coaxial methane-oxygen injector ports using a three-dimensional unsteady $k-\omega$ shear-stress transport detached eddy simulation (DES) method, a hybrid LES/RANS model, with a one-step chemical kinetic model. The triggered tangential and longitudinal instability modes are obtained for the 19-injector geometry with combustion chamber diameter of 43 cm (where first-tangential and first-longitudinal frequencies equate) by pulsing the injector mass flux. It is shown that an oscillating combustion-chamber flow can be triggered to a new mode with a larger disturbance amplitude. For the 30-injector combustion engine, the spontaneous longitudinal-mode and tangential-mode instabilities are observed. The strengths of the two instability modes alternate during the simulation time. Energy appears to transfer from one mode to the other and back again such that domination alternates between the two modes. As the mixture becomes less fuel rich and moves towards the stoichiometric value, the oscillation amplitude decreases. For the 82-injector combustion engine simulations of the Rocketdyne experiment [14], four different one-step chemical kinetic rates are simulated on the resolved scale to determine the effect of burning rate. When the normalized kinetic rate is one, implying the nominal Westbrook-Dryer rate, only the longitudinal-mode instability is observed. As the kinetic rate decreases, less of the combustion occurs upstream near the longitudinal-mode pressure antinode. The longitudinal-mode instability becomes weak and the first-tangential-mode instability emerges, which fits better with experiment. Thus, an implication is that use of simple kinetics at the resolved scale produces a burning rate which is too fast.

In recent years, combustion instability has been examined with more detailed description of the combustion process. However, in many hybrid LES/RANS modeling of the rocket combustion dynamics, such as those adopting the finite-rate chemistry assumption and the Laminar Closure Model (LCM) for the reaction source terms [15,16], the combustion process was modeled only on the resolved scale. Accuracy of such modeling is acceptable when a rocket combustor is characterized by non-premixed diffusion flames [17] although the sub-grid combustion behavior in turbulent flows is usually dominant in determining burning rate and energy-release rate. Due to the finite-rate chemistry assumption, most high-fidelity LES calculations of combustion instability, even those with turbulent combustion models [18,19], employed quite simple chemical mechanisms that involve few species and reaction steps. Only a limited number of studies, such as those conducted by Sardeshmukh et al. [20] for 2D axisymmetric and Harvazinski et al. [17] for fully 3D domain, employed the detailed GRI-Mech 1.2 mechanism to study longitudinal combustion instability in a single element rocket engine. Sardeshmukh et al. [20] observed an improvement in pressure oscillation amplitude compared to previous axisymmetric calculations performed by Harvazinski et al. [21] and Garby et al. [19]. However, these studies were computationally expensive because the authors employed finite-rate species transport approach with LCM, which directly transport all 31 species and integrate their chemical source terms.

In some later works, the sub-grid effect on combustion was considered without the finite-rate chemistry assumption, such as those [7–9] using the Steady Laminar Flamelet (SLF) combustion model [22,23]. Most recently, motivated by the findings of Sardeshmukh et al. [20], Nguyen et al. [24] developed a new 2D axisymmetric compressible solver using Delayed-Detached-Eddy-Simulation (DDES) turbulence model together with the compressible version [25,26] of the Flamelet Progress Variable (FPV) combustion model [27]. Based on the cost-effective combustion model, a detailed 27-species mechanism [28] was efficiently incorporated in simulations of combustion dynamics of a single-injector rocket engine. Consistent with findings in [20], the new solver predicted pressure fluctuation amplitude that is in good agreement with experimental measurement. In contrast to previous LCM simulations, computational cost associated with the new solver is much lower due to the FPV model. Subsequently, Nguyen and Sirignano [29], by examining in detail the flamelet solutions from the solver, found that local flame extinction and re-ignition was a major mechanism in driving the combustion instability. In the most unstable case, depending on the time in an oscillation cycle, the flame can either be attached to the backstep or lifted away from it. This complex flame dynamics cannot be observed by Pant et al. [30], despite the use of a complex chemical mechanism with the SLF combustion model. By parameterizing its flamelet solutions using the scalar dissipation rate instead of the progress variable used by the FPV, the SLF model could only access the stable burning branch. Therefore, the flame in these calculations was attached to the backstep where local extinction and re-ignition does not occur, leading to an under-prediction of the oscillation amplitude. Finally, Nguyen and Sirignano [31] compared spontaneous and triggered instability of the single element rocket engine. By applying an iso-thermal boundary condition, the spontaneous instability occurring in the chamber was suppressed. However, triggered instability could occur in the otherwise stable domain if sufficiently large perturbation, in the form of inlet mass flow rate disturbance, was introduced into the chamber.

As an advanced combustion model, the FPV model not only considers flame/turbulence interaction at sub-grid levels, but also restricts computational cost to minimum regardless of the incorporated chemistry accuracy. All of these advantages make the FPV model a perfect choice to address the challenges of balancing simulation fidelity and computational cost in numerical investigations of complex realistic rocket engines. To the best of our knowledge, there have been rare applications of FPV to combustion instability study of a multi-injector rocket engine like the one presented in this paper. Therefore, we extend our previous works and demonstrate one of the first endeavors in such cost-effective simulations and focus on analysis of the transverse instability behavior that are commonly seen with multiple injectors. Specifically, we perform a three-dimensional hybrid LES/RANS turbulent combustion simulation of a 10-injector rocket engine and investigate the spontaneous combustion instability using the efficient compressible

FPV combustion model and relatively detailed chemical reaction mechanism. Note that the system is fed with propellants in gaseous form as the focus of this paper is not on dense liquid or transcritical form injection although they are more common in practice. Furthermore, no works have made comparisons between the predictions with resolved-scale combustion modeling based on LCM versus sub-grid combustion modeling using FPV. Therefore, we also include such effort in this paper for the rocket engine configuration.

In the following sections, we will first describe the combustion models and then introduce the simulation tools that we developed recently. Based on the simulation results, we will discuss flamelet solutions at the high background pressures, partially premixed turbulent combustion, and combustion instability analysis for both the FPV and the LCM models. Finally, we analyze the resonance phenomenon inside the injectors.

2. The flamelet progress variable combustion model

2.1. The governing equations

For a mixture of multi-species, the Favre-filtered Navier–Stokes equations are written in the following conservative form as

$$\frac{\partial \bar{\rho}}{\partial t} + \frac{\partial \bar{\rho}\widetilde{v}_j}{\partial x_j} = 0 \tag{1}$$

$$\frac{\partial \bar{\rho}\widetilde{v}_i}{\partial t} + \frac{\partial \bar{\rho}\widetilde{v}_i\widetilde{v}_j}{\partial x_j} = -\frac{\partial \bar{p}}{\partial x_i} + \frac{\partial(\tau_{i,j} + \tau^R_{i,j})}{\partial x_j} \tag{2}$$

$$\frac{\partial \bar{\rho}\widetilde{h_a}}{\partial t} + \frac{\partial \bar{\rho}\widetilde{v}_j\widetilde{h_a}}{\partial x_j} + \frac{\partial \bar{\rho}\widetilde{K}}{\partial t} + \frac{\partial \bar{\rho}\widetilde{v}_j\widetilde{K}}{\partial x_j} - \frac{\partial \bar{p}}{\partial t} = \frac{\partial[\widetilde{v}_i(\tau_{i,j} + \tau^R_{i,j})]}{\partial x_j} + \frac{\partial}{\partial x_j}\left[\left(\frac{\lambda}{c_p} + \frac{\mu_t}{Pr_t}\right)\frac{\partial \widetilde{h_a}}{\partial x_j}\right] \tag{3}$$

where $\bar{\rho}$ is the filtered density, $\widetilde{v}_j$ is the filtered velocity vector and $\bar{p}$ is the filtered pressure. In the energy equation, $\widetilde{h_a}$ is the filtered total (or absolute) enthalpy, which is the summation of the filtered sensible enthalpy $\widetilde{h_s}$ and the filtered enthalpy of formation $\widetilde{h_c}$, while $\widetilde{K} = \frac{1}{2}(\sum_{j=1}^{n}\widetilde{v}_j\widetilde{v}_j)$ is the filtered kinetic energy. λ and C_p are the heat conductivity coefficient and the specific heat at constant pressure. Pr_t is turbulent Prandtl number. $\tau_{i,j}$ and $\tau^R_{i,j}$ are the molecular and turbulent stress tensors and expressed as $\tau_{i,j} = \mu(\frac{\partial \widetilde{v}_i}{\partial x_j} + \frac{\partial \widetilde{v}_j}{\partial x_i} - \frac{2}{3}\frac{\partial \widetilde{v}_k}{\partial x_k}\delta_{i,j})$ and $\tau^R_{i,j} = \mu_t(\frac{\partial \widetilde{v}_i}{\partial x_j} + \frac{\partial \widetilde{v}_j}{\partial x_i} - \frac{2}{3}\frac{\partial \widetilde{v}_k}{\partial x_k}\delta_{i,j}) - \frac{2}{3}\rho k\delta_{i,j}$ with μ and μ_t being the molecular and eddy viscosity. k is the turbulent kinetic energy. The detached-eddy simulation (DES) [32] based on the $k-\omega$ shear-stress transport (SST) [33] is adopted as the turbulence closure model. The eddy viscosity is calculated as $\mu_t = \frac{\rho a_1 k}{max(a_1\omega, \Omega F_2)}$, where a_1 and F_2 are a constant and a blending function in the $k-\omega$ SST model [33], ω and Ω are the specific dissipation rate and vorticity magnitude.

The DES model acts like a LES model away from walls and reduces to the $k-\omega$ SST model near walls. This is achieved by replacing the dissipation term $\beta^*\rho k\omega$ in the k−equation of the SST model with $\beta^*\rho k\omega F_{DES}$, which is essentially a modification of the embedded turbulent length scale. β^* is a constant of the model [33]. The DES limiter F_{DES} is given by:

$$F_{DES} = max\left(\frac{L_t}{C_{DES}\Delta}(1 - F_{SST}), 1\right) \tag{4}$$

where turbulent length scale $L_t = \frac{\sqrt{k}}{\beta^*\omega}$ is used in the near-wall RANS simulation, and the grid length scale $L_{grid} = C_{DES}\Delta$ is employed in the LES-like modeling away from walls. Δ is the maximum local grid dimension and the model constant C_{DES} is calibrated to be 0.61. The coefficient F_{SST} is selected to be the F_2 blending function of the SST model [32] in order to reduce the undesired influence of the DES limiter on boundary layers that usually associated with the model of Strelets [34] (when $F_{SST} = 0$). To facilitate using coarse mesh near walls and hence reduce computational cost, k, ω and the turbulent kinematic viscosity ν_T at walls are specified by wall functions. These boundary conditions are appropriate when a high Reynolds number turbulence model is used on a coarse mesh and the y^+ value is in the range $30 < y^+ < 200$.

2.2. The turbulent combustion model

For the computations of turbulent combustion in this paper, only the mean quantities are transported. Hence, the laminar flamelet solutions need to be convoluted with assumed probability density functions of the independent scalars, including mean mixture fraction $\widetilde{Z}$ and the mean variance of mixture fraction $\widetilde{Z''^2}$. The convolution generates flamelet libraries of mean quantities which can be accessed efficiently during the computation of the flow equations. In the FPV model, the flamelet tables are also parameterized by a mean reaction progress variable $\widetilde{C}$. In this paper, the progress variable is defined as the total mass fraction of four major species, which are CO_2, H_2O, H_2 and CO. Hence, a mean thermal and chemical quantity $\widetilde{\psi}_i$, such as composition or temperature, is given by

$$\widetilde{\psi}_i(\widetilde{Z}, \widetilde{Z''^2}, \widetilde{C}) = \int_0^1\int_0^1 \psi_i(Z, C)\tilde{P}(Z, Z''^2, C)dZdC \tag{5}$$

where $\tilde{P}$ is the PDF function for $\widetilde{\psi}_i$. The PDF for the progress variable is frequently assumed to be the Dirac δ function of C; thus, (5) is reduced to

$$\widetilde{\psi}_i(\widetilde{Z}, \widetilde{Z''^2}, \widetilde{C}) = \int_0^1 \psi_i(Z, \widetilde{C})\tilde{P}(Z, Z''^2)dZ \tag{6}$$

Finally, the β PDF is assumed for $\tilde{P}$, which gives

$$\tilde{P}(Z, Z''^2) = \frac{Z^{\alpha-1}(1-Z)^{\beta-1}}{\Gamma(\alpha)\Gamma(\beta)}\Gamma(\alpha+\beta) \tag{7}$$

where Γ is the gamma function. α and β are shape functions which are defined as $\alpha = Z\gamma$ and $\beta = (1-Z)\gamma$ with $\gamma = [Z(1-Z)/Z''^2] - 1 \geq 0$.

For compressible combustion, the tables should be generated at different background pressures and pressure should be included as an input to access the tables. Pecnik et al. [25] showed that the composition of the reacting mixture is not sensitive to the background pressure and only the reaction rate changes dramatically. This fact justifies the method of using tables under one background pressure (usually the averaged pressure) and rescaling the reaction rate for other pressures. In this paper, we adopt this approach to simplify preparation of the tables and the table lookup process.

At each time step in the CFD computation, the transport equations for scalars $\widetilde{Z}$, $\widetilde{Z''^2}$ and $\widetilde{C}$ are solved. When the Lewis number is equal to one, these equations are given as

$$\frac{\partial \bar{\rho}\widetilde{Z}}{\partial t} + \frac{\partial \bar{\rho}\widetilde{v}_j\widetilde{Z}}{\partial x_j} = \frac{\partial}{\partial x_j}\left[\left(\frac{\mu}{Sc} + \frac{\mu_t}{Sc_t}\right)\frac{\partial \widetilde{Z}}{\partial x_j}\right] \tag{8}$$

$$\frac{\partial \bar{\rho}\widetilde{Z''^2}}{\partial t} + \frac{\partial \bar{\rho}\widetilde{v}_j\widetilde{Z''^2}}{\partial x_j} = \frac{\partial}{\partial x_j}\left[\left(\frac{\mu}{Sc} + \frac{\mu_t}{Sc_t}\right)\frac{\partial \widetilde{Z''^2}}{\partial x_j}\right] + 2\frac{\mu_t}{Sc_t}\frac{\partial \widetilde{Z}}{\partial x_j}\frac{\partial \widetilde{Z}}{\partial x_j} - \bar{\rho}\widetilde{\chi} \tag{9}$$

$$\frac{\partial \bar{\rho}\widetilde{C}}{\partial t} + \frac{\partial \bar{\rho}\widetilde{v}_j\widetilde{C}}{\partial x_j} = \frac{\partial}{\partial x_j}\left[\left(\frac{\mu}{Sc} + \frac{\mu_t}{Sc_t}\right)\frac{\partial \widetilde{C}}{\partial x_j}\right] + \widetilde{\omega_C} \tag{10}$$

where $\widetilde{\chi}$ is the Favre-averaged scalar dissipation rate. By comparing the integral scalar time scale and the turbulent flow time scale, $\widetilde{\chi}$ is frequently expressed as $\widetilde{\chi} = C_\chi\frac{\tilde{\varepsilon}}{\tilde{k}}\widetilde{Z''^2}$ [22,23] with $\tilde{k}$ and $\tilde{\varepsilon}$ being the mean turbulent kinetic energy and mean turbulent dissipation. A constant value of 2.0 is often used for C_χ. The laminar and turbulent Schmidt number Sc and Sc_t are 1.0 and 0.7, respectively. The source term $\widetilde{\omega_C}$ in Eq. (10) is the reaction rate for the progress variable. It is the summation of the reaction rates for the individual species involved in the definition of the progress variable and is prepared in the flamelet tables.

The FPV approach is by nature a flamelet model. It also assumes that the chemical time scales are shorter than the turbulent time scales so that the flame can be viewed as a collection of laminar flamelets. For this reason, the FPV approach is regarded as assuming infinitely fast reactions. This assumption is valid in many turbulent combustion problems and the FPV approach has even been successfully applied to highly turbulent flames like Sandia Flames D and E as shown in the work by Ihme et al. [35,36]. In combustion instability problems, the time scales of dominant acoustics are associated with longitudinal and transverse flows in the combustion chamber, and hence are even larger than the turbulent time scales. This fact further justifies the use of the FPV approach in prediction of combustion instability.

It should be noted that ignition delay is an important factor for combustion instability. Sardeshmukh et al. [20] pointed out that ignition delay is closely related to mixing, local extinction and reignition, which are key to the instability mechanism. The timing of these events is directly coupled with the chamber acoustics in the unstable cases. The FPV model is quasi-steady; however, by inclusion of both the unstable and stable burning branches, it has been shown [27,29] to reflect very well the extinction, re-ignition, and associated flame-holding that occurs in a dynamic situation, such as turbulent combustion with or without large-amplitude acoustic oscillations. The use of the FPV model has been justified via comparison with a well known Purdue experiment [24,29,31,37,38]. Despite some shortcomings that have been well presented [29], the FPV approach is currently the best option available for connection with flow-field simulation as a sub-grid combustion model.

2.3. The laminar flame calculator

Here, the laminar flamelet solutions are generated using FlameMaster, an open source C++ program package for zero-dimensional combustion and one-dimensional laminar flame calculations [39]. The code can be used for steady and unsteady computations of premixed as well as non-premixed flames. For the methane/oxygen combustion that we consider, we use the module of the code that solves the steady flamelet equations in the mixture fraction space by assuming counterflow configuration. To run the code, a chemical mechanism and corresponding thermo and transport data are needed. The background pressure, composition and temperature on both the fuel and oxidizer sides are required. For each given stoichiometric scalar dissipation rate (χ_{st}), the code generates a flame solution in the form of distributions of temperature, composition, reaction rates and heat release rate in the mixture fraction space. Hence, the laminar flamelet solutions are already parameterized by the scalar dissipation rate and the mixture fraction.

Since chamber pressure in the current study is around 200 bar, a chemical mechanism suitable for high-pressure combustion is desired. We adopt a skeletal model of 12 species, which is generated by selecting relevant species and reaction pathways from version y of a 119-species Foundation Fuel Chemistry Model (FFCM-y) [40,41]. The FFCM models were recently developed with uncertainty minimization against up-to-date experimental data for the combustion of small hydrocarbon fuels. The models were tested for fuels, such as methane, over the pressure range of 10-100 atm. The 12-species skeletal model is called FFCMy-12 mechanism in this paper and the included species are H_2, H, O_2, O, OH, HO_2, H_2O, CH_3, CH_4, CO, CO_2, and CH_2O. Reaction rate constants in the model are optimized for the same wide range of pressure, using the FFCM-y computation results as the optimization targets. Note that ignition delay is among the optimization targets and it is identified an key factor for combustion instability. Sardeshmukh et al. [20] pointed out the global one-step and two-step kinetics have too few tunable parameters to calibrate for targets like ignition delay over a wide range of operating conditions. The FFCMy-12 mechanism is much more detailed and has sufficiently many tunable parameters which support wide calibration range. Meanwhile, the mechanism is still compact in size compared to even more detailed kinetics. For these reasons, the FFCMy-12 mechanism is an cost-effective choice for high-pressure combustion simulation and combustion instability analysis in this paper.

2.4. Numerical solver

To numerically simulate combustion using the FPV approach, a C++ code is developed based on OpenFOAM 4.1. There is a similar open-source code called flameletFoam [42]. However, it only provides the original version of the flamelet model. The progress variable approach is not available. Moreover, tabulated temperature is directly used without any correction, which makes the code applicable only to incompressible combustion. Last but not least, since the code is based on the outdated 2.4 version of OpenFOAM, selection of turbulence model is limited. For example, the hybrid RANS/LES based on the SST $k-\omega$ model is not available. In the newly developed code, transport Eqs. (8), (9) and (10) are solved for $\widetilde{Z}$, $\widetilde{Z''^2}$ and $\widetilde{C}$. These quantities are then used to retrieve composition, $\widetilde{\omega_C}$ and h_c from the tables. Since $\widetilde{\omega_C}$ is tabulated only for background pressure of 200 bar, it is rescaled using a power law for other values of pressure. We will discuss it in the next section. In this paper, the energy equation is solved for h_a. After that, sensible enthalpy h_s is obtained by subtracting h_c from h_a. Temperature is then calculated from sensible enthalpy h_s using the Joint Army Navy NASA Air Force (JANAF) polynomials and tables of thermodynamics [43].

As temperature for each individual species in the flamelet is typically higher than its critical point of gas, all species are in the gaseous phase. The ideal-gas equation of state (EOS) is employed. Pressure and temperature of the burning mixture are both high in the present case. At these conditions, the perfect-gas law describes the real gases well. Hence, the EOS for real gas is replaced by the ideal-gas EOS for simplicity without significant loss of accuracy in the current computations. The reacting-mixtures model is adopted to calculate the properties of the mixture. Since compressibility is considered in the combustion simulation, a density-based thermodynamics package is used. The differencing schemes are second-order accurate in both space and time. Implicit backward differencing is selected for time discretization. For spatial discretization, Gaussian integration is chosen. Second-order derivatives are approximated using linear interpolation from cell centers to cell faces.

Numerical studies of combustion instability are computation-intensive, and thus affordability of modeling approaches is a major concern. For comparison, we also implement the one-step-kinetics (OSK) method, another completely affordable approach, which applies the LCM combustion model and only considers the one-step global chemical reaction, by a canonical OpenFOAM code called rhoReactingFoam. The turbulence model, thermodynamics model, and numerical schemes remain the same as those used with the FPV model. Xiong et al. [11–13] used this same OSK approach in simulations concerning rocket engines with 10, 19, 30, and 82 co-axial injectors. The code validity and accuracy were verified in those simulations, especially through the favorable comparison with the 82-injector Rocketdyne experiment based on a properly reduced global reaction rate in the OSK model. The fact that the global reaction in the OSK model has to be slowed indicates the need to use a more detailed chemical mechanism, which can be efficiently integrated in combustion simulations by the FPV approach. Although the configurations with fewer (10, 19 and 30) injectors have no matching experiments in the literature, there still exist the key features of the combustion dynamics in a multi-injector rocket engine. Meanwhile, the computational cost of the numerical analysis is reduced due to simpler geometry with fewer injectors. Last but not least, the flow within the injector ports can be simulated with a better resolution compared to that for configurations with many injectors [11–13]. To best leverage these benefits, a ten-injector rocket engine is examined in this paper.

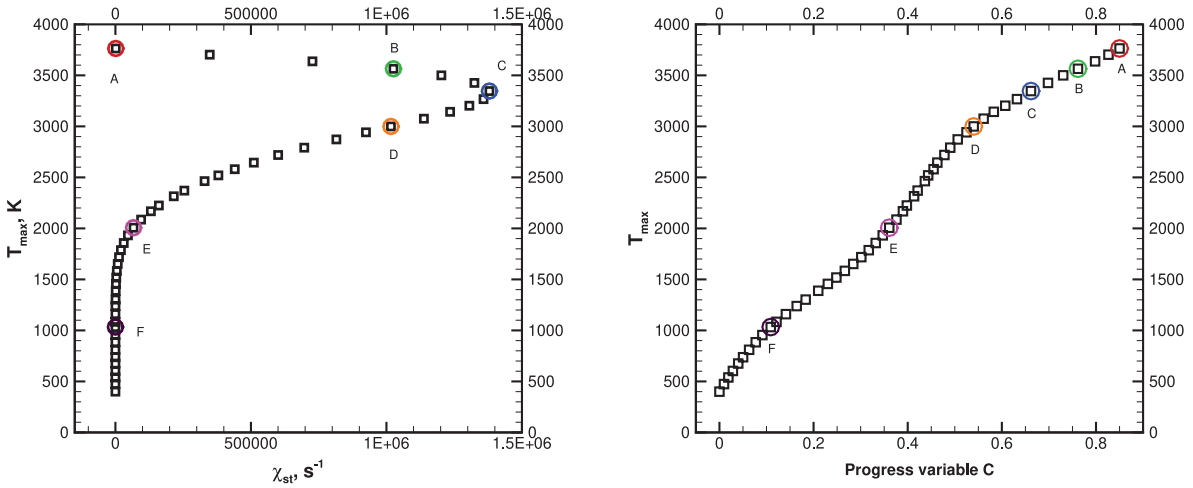

(a) S curve (b) T_{max} vs. C

Fig. 1. Steady flamelet solutions for methane/oxygen combustion with $T_f = T_o = 400$ K at $p = 200$ bar.

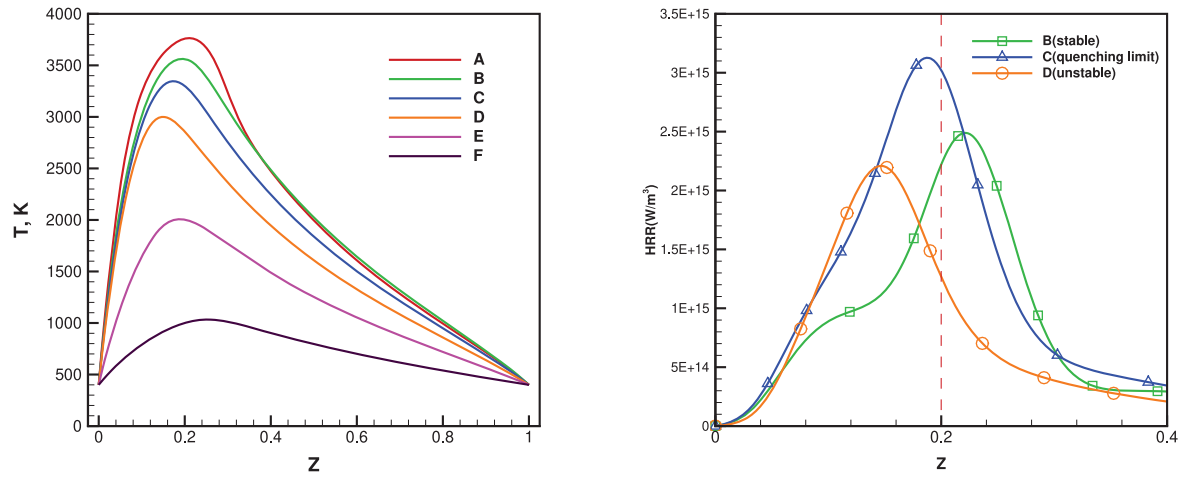

(a) $T(Z)$ at various progress variable (b) $HRR(Z)$ at and near quenching limit

Fig. 2. Representative flamelet solutions over the complete S-curve at $p = 200$ bar.

3. Results and discussion

3.1. The flamelet solution

To apply the FPV model to the turbulent combustion of the ten-injector chamber, steady-state laminar flamelet solutions are obtained first by feeding the FFCMy-12 mechanism into the FlameMaster code. The fuel and oxidizer are pure methane and oxygen, respectively; operating pressure is 200 bar; and the temperature on both fuel and oxidizer sides is 400 K. Fig. 1(a) shows the maximum temperature in a flamelet solution as a function of χ_{st}, which is frequently called the S curve. It is multi-valued as mentioned above and only the upper branch can be used in the SLF model. In the progress variable approach, the curve becomes single-valued and monotonic as shown in Fig. 1(b). Hence, both the upper and lower branches can be explored in the flow computation. Note that the branch composed of pure mixing solutions only is not shown underneath the unstable burning branch in the S curve. Obtaining these solutions is challenging using the software FlameMaster due to the targeted high pressure in this paper as convergence issues are encountered. However, the burning rate in the pure mixing solutions is zero. Compared to the shown stable and unstable burning branches in Fig. 1(a), the pure mixing solutions have much less impact on the CFD modeling of the reacting flow and thus they are not considered in the combustion simulation.

Selected particular flamelet solutions along the S-shaped curve are shown in Fig. 2(a). The mixture fraction is zero on the oxidizer side and one on the fuel side, indicating the flow is solely composed of the oxidizer or the fuel. The top two curves (A and B) are on the upper branch of the S-shaped curve and represent stable burning flamelet solutions. The third curve (C) is the flamelet solution at the quenching limit. The next three curves (D, E, and F) below it are on the lower branch of the S-shaped curve and represent unstable burning flamelet solutions. These solutions are classified as unstable due to their sensitivity to small perturbations and easily moving either toward the stable upper branch or toward a stable quenched solution [44].

Fig. 2(b) shows the heat release rate (HRR) of the stable burning solution B, the quenching limit solution C and the unstable burning solution D. Note that solutions B and D are obtained using approximately the same stoichiometric dissipation rate. The vertical dash line marks the stoichiometric mixture fraction $Z_{st} = 0.2$. A region immediately on the left is the approximated oxidation layer [45]. In the unstable burning limit, heat is intensively released on the fuel-lean side within the oxidation layer. This region of intense HRR is mainly associated with the reactions involving H_2O and CO_2. In the stable burning limit,

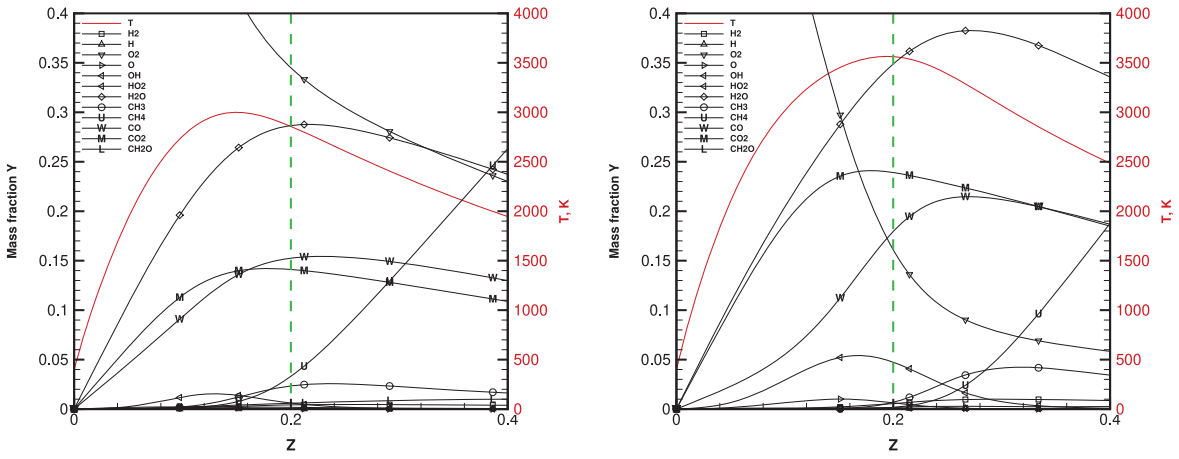

(a) Unstable (b) stable

Fig. 3. Flamelet solutions near the quenching limit at $p = 200$ bar.

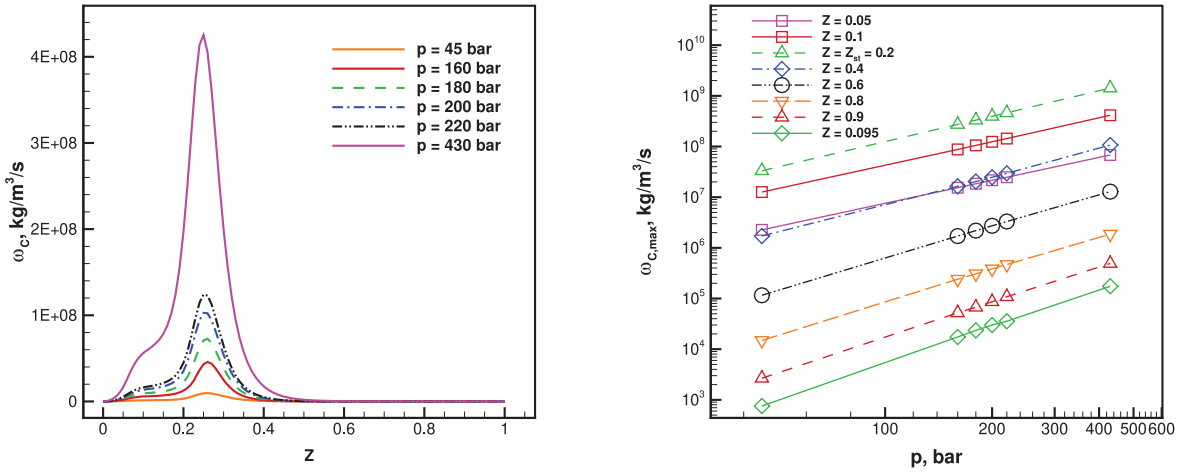

(a) ω_C vs. Z (b) $\omega_{C,max}$ vs. p

Fig. 4. Pressure effect on the reaction rate for the progress variable ω_C.

however, the strong HRR region moves across the stoichiometric line to the slightly fuel-rich side. Reactions in this branch are much more stable and the reduction of CH_4 accounts for a larger fraction of the total HRR. Fig. 3 shows mass fractions of individual species and temperature profiles as functions of the mixture fraction on the left for the unstable burning flamelet solution B and on the right for the stable burning flamelet solution D. In both cases, due to extremely high scalar dissipation rates in the reaction zone (where characteristic diffusion time is quite small), there is remarkable reactant leakage through the zone, as shown in Fig. 3. In the stable burning case, oxygen is consumed faster across the oxidation layer. Hence, oxygen leakage to the fuel-rich side is less. Despite the much higher background pressure in this paper, The flame structures described above are still qualitatively similar to those reported by previous work for methane/air diffusion flame [29,45].

In this paper, the flamelet solutions for the background pressure of 200 bar are actually used only in the table-look-up process during flow computations. Our observation confirms that composition changes little with pressure, whereas the reaction rate for the progress variable (ω_C) varies dramatically. Fig. 4(a) shows ω_C as a function of Z for different pressures with C fixed at the maximum value 0.85, which corresponds to flamelet solutions at chemical equilibrium.

Plotted in a log–log graph as shown in Fig. 4(b), $\omega_{C,max}$ changes linearly with pressure, indicating that ω_C is approximately a power function of pressure. $\widetilde{\omega_C}$ at a given pressure $\bar{p}$ can be obtained by rescaling $\widetilde{\omega_{C_0}}$ at pressure of 200 bar ($\bar{p_0}$) as

$$\widetilde{\omega_C} = \widetilde{\omega_{C_0}} \frac{\bar{p}^{\eta}}{\bar{p_0}^{\eta}} \tag{11}$$

Note that the power η changes with not only Z but also its variance Z''^2. This is a natural result of $\widetilde{\omega_C}$'s dependence on Z''^2, which is mathematically described by (6) and (7) with the chemical quantity $\widetilde{\psi}_i$ being the progress variable reaction rate. Fig. 4 actually assumes zero Z''^2. At a different value of Z''^2, we found the power law is still a good approximation given a different power η. Hence, for any combination of Z and Z''^2, the power law (11) can be used as a regression function to calculate the power η. Once the power is obtained, for a fixed value of Z''^2, a quadratic regression function is found to be cost-effective to describe the dependence of the power on Z. The three coefficients of the quadratic function are then calculated for different values of Z''^2.

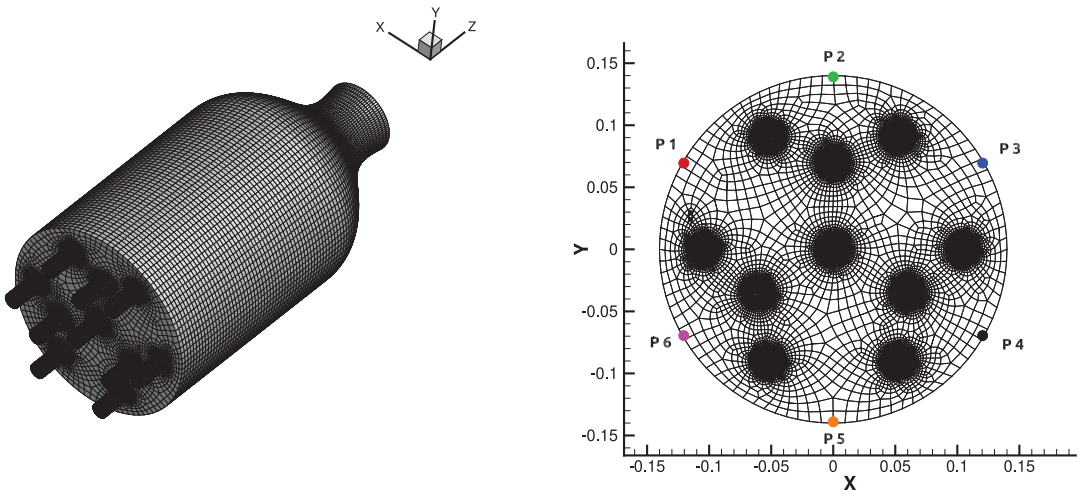

(a) Isometric view (b) Front view

Fig. 5. Unstructured mesh for the ten-injector rocket engine.

A linear regression function is found to be cost-effective to describe the dependence of these coefficients on Z''^2. We also found Z''^2 seldom exceeds 0.11 in simulation. The simple linear function of Z''^2 seems to be able to cover the narrow range of Z''^2 variation well. The final approximation of η is given in Eq. (12).

$$\eta = (3.0882Z''^2+0.0101)Z^2+(-3.7851Z''^2+0.9567)Z+(0.6638Z''^2+1.4589) \tag{12}$$

Compared to the direct interpolation of the reaction rate based on pressure, the use of rescaling law (11) and (12) avoids parameterization of the flamelet tables with respect to pressure and reduces the effort of table look-up process in combustion simulation. A similar approach was reported by Pecnik et al. [25] for hydrogen combustion. Our work differs from it in two ways: (1) The rescaling law is determined for methane combustion under much higher background pressure; (2) the power's dependency on both Z and Z''^2 is considered.

3.2. Combustion simulation of a ten-injector liquid rocket engine

In this paper, turbulent combustion is numerically simulated in a liquid rocket engine with an convergent-divergent nozzle and ten coaxial fuel/oxidizer injectors [11]. The three-dimensional unstructured mesh with 1.608502×10^6 grid cells is shown in Fig. 5(a). The combustion chamber has a diameter of 28 cm and a length of 53 cm. The distance between the injector plate and the choked nozzle is 33 cm. One of the ten coaxial injector ports mounted into the injector plate is located at the center. Three injector ports are equally distributed on the ring of radius 7 cm. The remaining six ports are evenly positioned on an outer ring of radius 10.5 cm. In the longitudinal direction, 55, 40 and 10 grid cells are distributed in the combustion chamber, nozzle and injector, respectively. In the radial direction of the combustion chamber, depending on whether a non-central injector falls in, there are about 40 or 80 grid cells. Note that the main objective of this paper is to predict the combustion instability behavior. For this purpose, the mesh is carefully generated to capture the major burning of fuel in the mixing layer between the two coaxial streams. Hence, as shown in Fig. 5(b), the grid points are clustered in those areas and dispersed in the rest regions to reduce computational cost. The resolution of this mesh is further justified in the discussion of computational results. The oxidizer, which is pure oxygen, is injected through the center of each coaxial port. The fuel, which is pure methane, is injected through the outside annulus. The mass fluxes for the fuel and oxidizer are fixed at 15 kg/s and 60 kg/s, respectively, leading to a propellant injection at the stoichiometric ratio. The diameter of the fuel injector is 2.2 cm and that of the oxidizer is 1.96 cm. The thickness of the inner channel lip is 0.2 mm. It is known that the flame anchoring and combustion instability are sensitive to the lip thickness and other designs like the lip recess [46]. However, discussion on these topic is beyond the scope of this paper. Under nominal injection conditions, the jet velocities for the fuel and oxidizer are 229 m/s and 97 m/s, respectively. The associated head losses are 5% (for oxidizer jets) and 13% (for fuel jets) of the chamber mean pressure for the OSK simulation and increase for the FPV model as the chamber pressure drops due to more realistic (lower) prediction of temperature. These pressure drops might be insufficient to decouple the upstream dome and feeding system from the combustion chamber [47] in acoustic resonance. However, for a multi-injector rocket engine configuration with typical upstream propellant feeding system, findings from some experiments and high-fidelity simulation [7] showed that, no matter which thermal-acoustic mode dominates in the combustion chamber, there is little acoustic activity inside the fuel injectors (thin concentric outer tubes) while the chamber instability mode is strongly coupled with a longitudinal mode of the oxidizer injectors (thick core tubes). Pressure oscillation in the upstream domes for the fuel and oxidizer is quite weak compared to that in the oxidizer injectors especially when a transverse mode dominates in the chamber. These facts suggest an acoustic decoupling between the chamber and the upstream devices that feed the injectors in a multi-injector configuration where transverse chamber instability mode is commonly found. The CVRC experiments [48] also revealed significant impact of the oxidizer injector length on the acoustic activity of the combustion chamber, confirming the strong acoustic coupling between the chamber and the oxidizer injector. Without the upstream feeding system, numerical analysis of the single injector engine in the CVRC experiments [24] and a multi-injector configuration in the Rocketdyne experiment [13] all matched well with data on the type and frequency of the dominant instability mode. Hence, the upstream feeding system is not considered in this paper to reduce computational cost.

Temperature at both the fuel and oxidizer injector inlets is 400 K. The injection of propellants at 400 K can match practice where propellants flow through the combustion-chamber walls, serving as a coolant before injection in a manner that brings the system closer to adiabatic operation. The use of LOX as a coolant for combustion chamber might

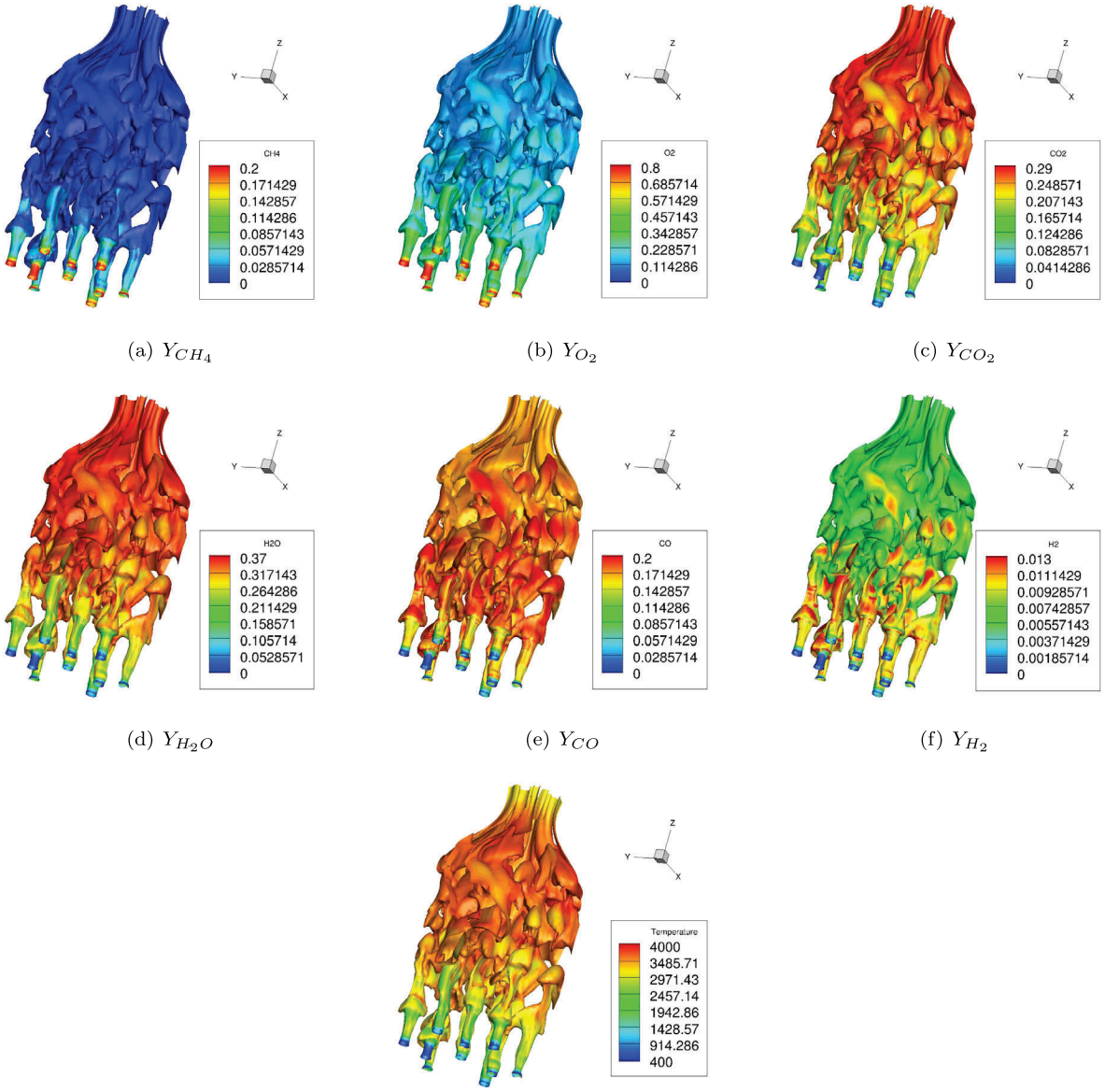

(a) Y_{CH_4} (b) Y_{O_2} (c) Y_{CO_2}

(d) Y_{H_2O} (e) Y_{CO} (f) Y_{H_2}

(g) T, K

Fig. 6. Instantaneous isosurface of $Z_{st} = 0.2$ colored by mass fraction of major reaction species and temperature for the FPV model at $t = 50$ ms.

be less common. However, it occurred in the past [49–52] and draws interest recently [53,54]. For the low-temperature flows inside injectors, ideal-gas EOS is not an accurate approximation. However, for the major portion of the volume of the chamber and nozzle, real-gas effects can be considered negligible. For this reason, ideal-gas EOS is applied everywhere in the rocket engine to reduce computational cost.

On the walls, the no-slip boundary condition is applied and the normal pressure gradient is zero. Furthermore, the walls are assumed adiabatic and free of surface chemistry. At the injector inlets, the mean mass fluxes for methane and oxygen are fixed, yielding the steady-state mass flow rate for sonic throat of the nozzle. The wave-transmissive boundary condition is used at the outlet boundary due to the supersonic nozzle flow. This boundary condition prevents waves from propagating backward into the system and hence guarantees that neither shock nor backflow occurs in the combustion.

The initial pressure in the combustion chamber is 200 bar. The simulations start from an initially quiescent flow at 3229 K and a chamber pressure at 200 bar. The higher chamber temperature shortens the ignition process and reduces the computational time as no explicit ignition model is included in the current simulation.

Fig. 6 shows the instantaneous isosurface of the stoichiometric mixture fraction $Z_{st} = 0.2$ colored by the mass fraction of the major species in the reactions and temperature for the FPV model. Both CH_4 and O_2 are consumed fast downstream of the injector plate, producing most of the CO and H_2 in the upstream half of the combustion chamber. Remarkable reduction of CO and H_2 occurs in the downstream half of the combustion chamber as further oxidation of the two intermediate species greatly outweighs their replenishment from the burning fuel, which is hardly seen in the same region. However, the continued oxidation of CO and H_2 in the downstream half of the combustion chamber and the exhaust nozzle leads to the largest local accumulation of the final products CO_2 and H_2O. The temperature reaches a maximum as the mixture is about to enter the nozzle due to the continued heat release of the lasting oxidation process. However, the hot mixture

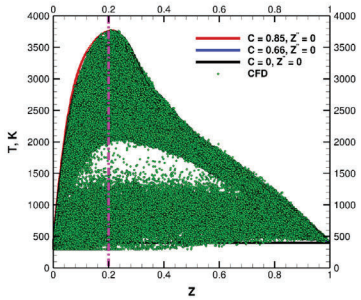

(a) T vs. Z at $z = 1$ cm

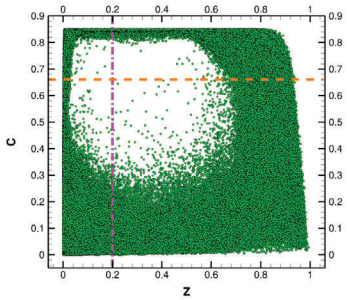

(b) C vs. Z at $z = 1$ cm

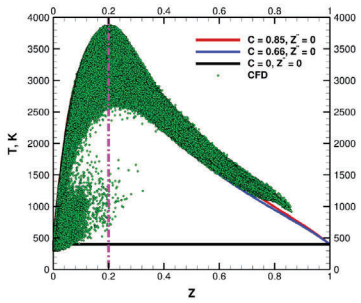

(c) T vs. Z at $z = 4$ cm

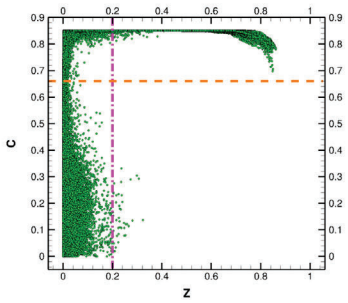

(d) C vs. Z at $z = 4$ cm

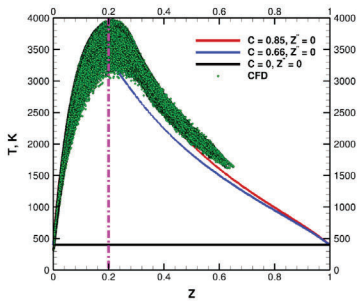

(e) T vs. Z at $z = 15$ cm

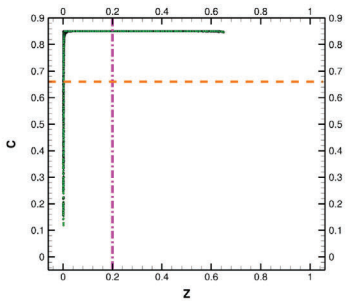

(f) C vs. Z at $z = 15$ cm

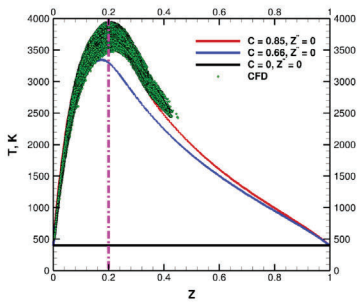

(g) T vs. Z at $z = 33$ cm

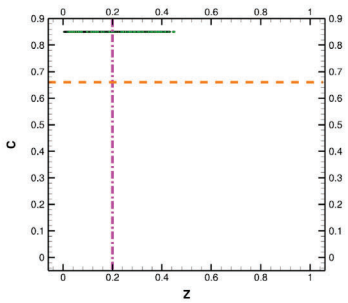

(h) C vs. Z at $z = 33$ cm

Fig. 7. Scatter plot of the flamelet solutions used in CFD on cross section planes.

cools in the entire nozzle, which is accompanied by the monotonic pressure drop and continued flow acceleration to supersonic speed. The instantaneous isosurface represents the dynamic structures in the flow associated with the propellant jets, indicating substantial turbulence and chemistry produced dilatation. One can observe the propellant jet structures close to the injector, and a rapid transition towards a remarkably disorganized flow. This highly turbulent flow interacts with the reactive layer and wrinkles the flame front. As turbulence enhances mixing, the reaction layer is thickened as shown in Figs. 9(a) and 9(d).

Fig. 7 shows scatter plots of the actual flamelet solution points that have been explored by the flow computations. Each of the green points represents a flamelet solution. As references, the laminar flamelet solutions for equilibrium burning, quenching limit and pure mixing are also plotted for background pressure of 200 bar. Some scatter points

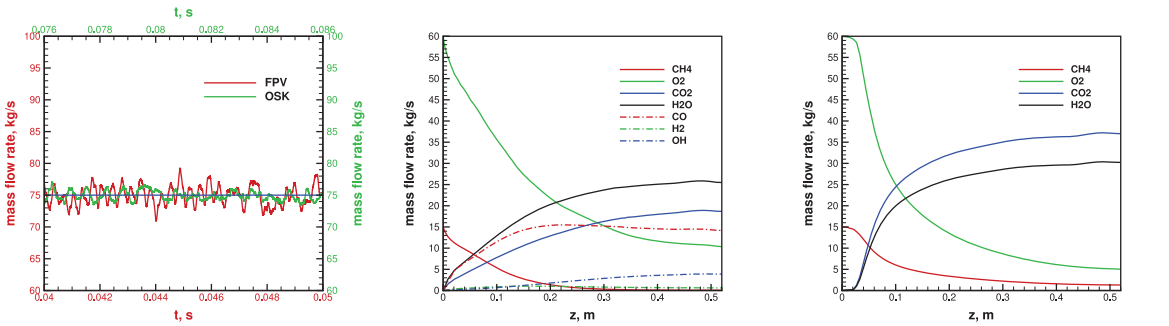

(a) Time history of the total $\dot{m}$ at the nozzle outlet

(b) Time-averaged $\dot{m}$ of individual species vs. axial position for the FPV model

(c) Time-averaged $\dot{m}$ of individual species vs. axial position for the OSK model

Fig. 8. Cross-sectional mass flow rate $\dot{m}$ as functions of time and axial position.

may not appear in the region enveloped by these reference solutions. A major reason is that the computed temperature may differ from that in the flamelet solutions due to compressibility. The pink dash-dot line separates the fuel-lean ($Z \leq 0.2$) and fuel-rich ($Z \geq 0.2$) burning regions. The quenching limit for the current case is $C = 0.66$. The orange dash line divides the stable ($C \geq 0.66$) and unstable ($C \leq 0.66$) burning branches. Along the mean flow direction/axial direction, local fuel-rich burning becomes more and more stable, the locally unstable burning tends to be fuel-lean. Near the exhaust nozzle, both fuel-rich and fuel-lean burnings are stable.

For comparison, we also implement the OSK model [11] in our computations. Since only three species equations are solved with this combustion model, the overall computational cost is similar to that of the FPV model. This fact seems to make the comparison a fair one although the two approaches differ in both chemistry accuracy and presence of the flame/turbulence subgrid interaction. The work presented in this paper is part of our series of efforts on cost-effective numerical analysis of combustion instability for multi-injector rocket engines. We reported computational results using the OSK approach previously and currently seek improved simulation fidelity for the same configuration while maintaining the minimum computational cost. For these reasons, we make direct comparison between the OSK approach and the FPV model equipped by a relatively detailed chemical mechanism. As shown in Fig. 8(a), the total mass flow rate at the nozzle outlet remains fluctuating around the value at the injector inlets (blue line) with notable amplitude in the last ten milliseconds. The limit-cycle behavior indicates that combustion instability occurs. Figs. 8(b) and 8(c) show that the OSK model predicts an evident mixing region immediately downstream of the injector plate. Within this region, the global reaction is weak. After sufficient mixing is achieved, the fast global reaction takes place and the major production of CO_2 and H_2O is completed within the upstream half of the combustion chamber. For the FPV model, fast dissociation of the fuel and further reactions are found just downstream of the injector plate as the chemical time scale is assumed to be much less than the turbulent time scales in the combustion model. Throughout the upstream half of the combustion chamber, lasting dissociation and oxidation of the fuel lead to continued accumulation of the major species including CO, CO_2, H_2, H_2O and OH. However, the mass flow rates of CO and H_2 start to decrease in the middle of the combustion chamber and they continue reducing further downstream. One of the two reasons is the nearly full consumption of the fuel beyond the cross-sectional plane at the chamber midpoint. The oxidation of the carbon element into CO and H_2 generation from the dissociation of the fuel almost completely stopped. The other reason is that, at the same time, further oxidation of CO into CO_2 continues, as does the oxidation of H_2 into OH and H_2O. For the reacting flow in the entire rocket engine, the global production rates of CO_2 and H_2O are lower in the FPV model compared to the OSK model as the two species are found with larger mass flow rates in the exhaust nozzle for the latter model. Another major difference is that significant oxidation and hence heat release occur in the entire rocket engine including the downstream half of the combustion chamber for the FPV model. For the OSK model, the evident reaction is only found in the upstream half of the combustion chamber. This major difference suggests distinct acoustic instability behavior between the two models as different locations of significant heat release are predicted by the two models.

Fig. 9 shows the time-averaged contours over the last ten milliseconds. The exhaust nozzle is choked with both combustion models. There is some unburnt fuel in the downstream part of the combustion chamber and the exhaust nozzle for the OSK model. Temperature is overpredicted in the combustion chamber by the OSK model due to the one-step reaction assumption, which is unrealistic because of lack of intermediate chemical reaction steps and hence missing dissociation. Despite the large temperature error, the OSK is completely affordable for simulations of complicated configurations of realistic rocket engines like the one studied in this paper. Note that, in the OSK approach, only three species transport equations are added into the system in addition to the flow governing equations and the system stiffness is low. Combining LCM model with more accurate chemistry helps to reduce error of temperature prediction. However, as more species are involved, computational cost grows fast due to solving more species transport equations. Furthermore, the system becomes very difficult to solve due to rapidly increased system stiffness, which makes the approach even unaffordable. Considering this fact and its lack of flame/turbulence interaction at subgrid levels, we choose not to explore further with LCM for realistic temperature prediction in this paper. The temperature prediction using the FPV model is more accurate because of the use of relatively detailed chemical kinetics and the built-in subgrid turbulence modeling for the chemical reactions in the FPV model.

Figs. 8 and 9 also suggest distinct combustion efficiency predicted by the two combustion models. Dissociation of propellant and reaction of intermediate species are considered with the current FPV model, leading to lower temperature, CO_2 concentration and production rate in the chamber, which are all indicators of lower but more realistic combustion efficiency.

To identify levels of local premixed flames and local diffusion flames, the following simple flame index can be defined:

$$FlameIndex = \omega_T \frac{\nabla Y_{CH_4} \cdot \nabla Y_{O_2}}{\left|\nabla Y_{CH_4}\right| \cdot \left|\nabla Y_{O_2}\right|} \tag{13}$$

Aligned gradients of the fuel mass fraction and the oxidizer mass fraction produce positive values of the flame index, which indicates premixed flames. When the two gradients are generally in the opposite direction, the flame index becomes negative, which suggests non-premixed or diffusion flames. As shown in Fig. 10, although the

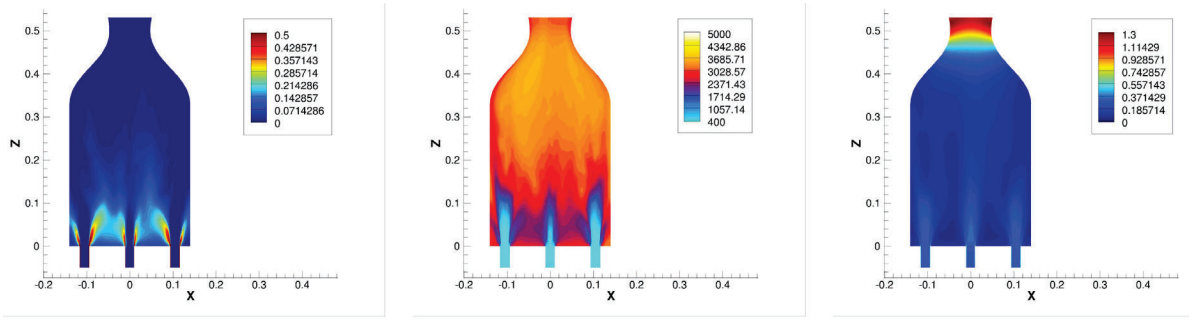

(a) $\bar{Y}_{CH4}$ for FPV (b) $\bar{T}$, K for FPV (c) $\overline{Ma}$ for FPV

(d) $\bar{Y}_{CH4}$ for OSK (e) $\bar{T}$, K for OSK (f) $\overline{Ma}$ for OSK

Fig. 9. Time-averaged contours on the $y = 0$ cm meridian plane.

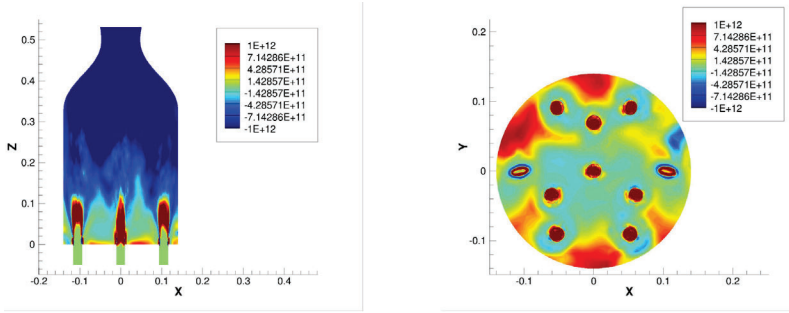

(a) $y = 0$ cm plane for FPV (b) $z = 4$ cm plane for FPV

(c) $y = 0$ cm plane for OSK (d) $z = 4$ cm plane for OSK

Fig. 10. Time-averaged flame index.

fuel and oxidizer just begin to mix after they enter the combustion chamber, the current computation using the FPV model shows partially premixed combustion. Note that there is a contradiction with the use of the FPV model which is constructed on the assumption of a diffusion flame but yet yields results for premixed flames in some cases. The simulation by the OSK model also shows partially premixed flames. In the surrounding region of the propellant jets, premixed flames dominate for both combustion models. However, Figs. 10(a) and Figs. 10(c) show

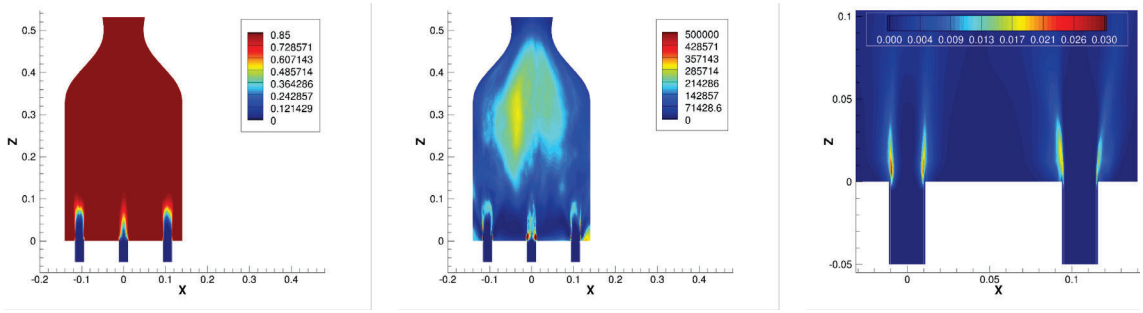

(a) $\overline{C}$ (b) $\overline{\omega_C}$, $kg/m^3/s$ (c) $\overline{Z''^2}$

Fig. 11. Time-averaged contours on the $y = 0$ cm meridian plane for the FPV model.

Table 1
Comparison of computational cost between FPV and OSK models.

	FPV	OSK
CFL	1	1
Test time interval (ms)	3.0×10^{-1}	4.0×10^{-1}
Number of time steps	1004	858
Average time step (ms)	2.99×10^{-4}	4.66×10^{-4}
CPU time (s)	9.6352×10^{3}	1.68552×10^{4}
CPU time/time step (s)	9.597	19.645
Total CPU time for LCO of 10 ms (s)	3.2117×10^{5}	4.2138×10^{5}

that the OSK model predicts strong premixed flames away from the injector lips while the FPV model favors strong premixed flames that are attached to the injector lips. This is consistent with the observations from Figs. 8(b) and 8(c) that significant one-step global reaction in the OSK model requires sufficient mixing before taking place and the FPV model assumes infinitely fast reactions. The combustion instability analysis in the next subsection shows that the dominant instability mode has pressure antinodes near the injectors. It was reported in previous work [12,24,29] that large-amplitude pressure oscillation enhances flow mixing and increases burning rate. This explains the dominance of the premixed flames in those regions. According to Seshadri and Peters [45], a small diffusion-controlled reaction layer exists around the stoichiometric mixture fraction on the fuel-rich side, which might occur adjacent to the premixed fuel-rich flames. As shown by Fiorina et al. [55], the flame index defined here cannot adequately distinguish this thin region. For the current FPV model which incorporates a relatively detailed mechanism, the flame index fails to well represent the flame behaviors as the dot products are taken only for global reactant gradients. For OSK, the flame index definition seems to be fit but the flame behaviors are not accurately predicted due to lack of intermediate chemical steps. The contours on the $z = 4$ cm plane reveal a key feature of some near-wall flames that is often associated with nearby pressure nodes in combustion instability. In Figs. 10(b), the premixed flames surrounding the left-most and the right-most injectors are noticeably stretched almost in the same direction, indicating transverse velocity fluctuation in the direction orthogonal to the stretch. Such flattened flames are called the "N-flame" by Urbano et al. [7]. In addition, the stretched premixed flames are further enclosed by flattened diffusion flames. At the locations corresponding to the rest injectors, only premixed flames are significant and their round shapes are maintained. On the same cross-sectional plane, similar premixed flame patterns are observed in Figs. 10(d) for the OSK model except that the "N-flame" is less stretched, indicating a slight azimuthal shift of the pressure nodes. The stretched premixed flames are not found surrounded by the flattened diffusion flames on this plane but it occurs on further downstream planes, which can be verified in Figs. 10(c). We also found some propellant escapes from the near-injector region as shown in Figs. 8(b) and 8(c). Thermal-acoustic analysis in the next subsection shows that pressure oscillation is significantly weakened starting one-third chamber length from the injector plate. It has little effect on fostering mixing of the leaked propellants. This is consistent with the finding that the diffusion flames prevail there. In the further downstream region near the nozzle entrance, although there still exists a very small leakage of propellants, they barely react in both the FPV and OSK simulations. Hence, identification of flame type in this region is not reliable using the flame index as it is defined upon gradient of propellants only. Note that for the OSK simulation, since intermediate chemical steps are missing, there is no burning at all in this region. For the FPV simulation, the reactions are among intermediate species rather than the propellant.

To provide more insight into the flame anchoring, contours of the time-averaged progress variable and its reaction rate are shown in Figs. 11(a) and 11(b). The premixed flame is anchored in the fuel/oxidizer shear layers. The Reynolds numbers of the oxygen and methane jets are 1.45×10^7 and 3.16×10^6, respectively. The current mesh is not able to adequately resolve the broad range of scales near the jets. However, the focus of this paper is the application of the FPV model to combustion simulation and more importantly the analysis of the resulting spontaneous thermal-acoustic instability. The current mesh is carefully generated to balance accuracy and computational cost. Despite the low total number of grid cells, the current mesh clusters grid cells in the jet regions and seems to be able to roughly predict effects of shear layer dynamics and unsteady mixing. Nguyen and Sirignano [29] pointed out that turbulent mixing and turbulence/flame interaction of the mean mixture fraction Z are modeled by solving equation of its variance Z''^2. Fig. 11(c) shows the contour of time-averaged Z''^2 in the exit vicinity of the central and an outer-annulus injectors. The present simulation finds that relatively large and fluctuating Z''^2 appear in the fuel/oxidizer shear layers, reflecting active unsteady mixing and shear-layer/flame interaction in the region. In principle, low grid resolution in the flame-anchoring region will effectively mischaracterize the flame structure and hence the combustion instability. However, Nguyen and Sirignano [31] pointed out that relatively coarse mesh of roughly 60,000 cells in axisymmetric simulations can still reasonably capture the correct unstable behavior of the Purdue CVRC experiments. Xiong et al. [11] performed the grid independence study for a 19-injector configuration and found further mesh refinement has little impact on pressure oscillation frequencies with the OSK approach. The resolution of the present mesh is about identical to that for the 19-injector configuration. It should be sufficient for the combustion instability study in this paper. Note that, for the FPV model, the time and length scales associated with the relatively detailed chemical kinetics are handled by the adaptive mesh algorithm of the software Flamemaster when the flamelet solutions are calculated. The time and length scales embedded in the governing equations of the FPV model are identical to those associated with the flow governing equations. Hence, the FPV model introduces no new (small) time and length scales. The mesh with resolution justified for the OSK model should also work well for the

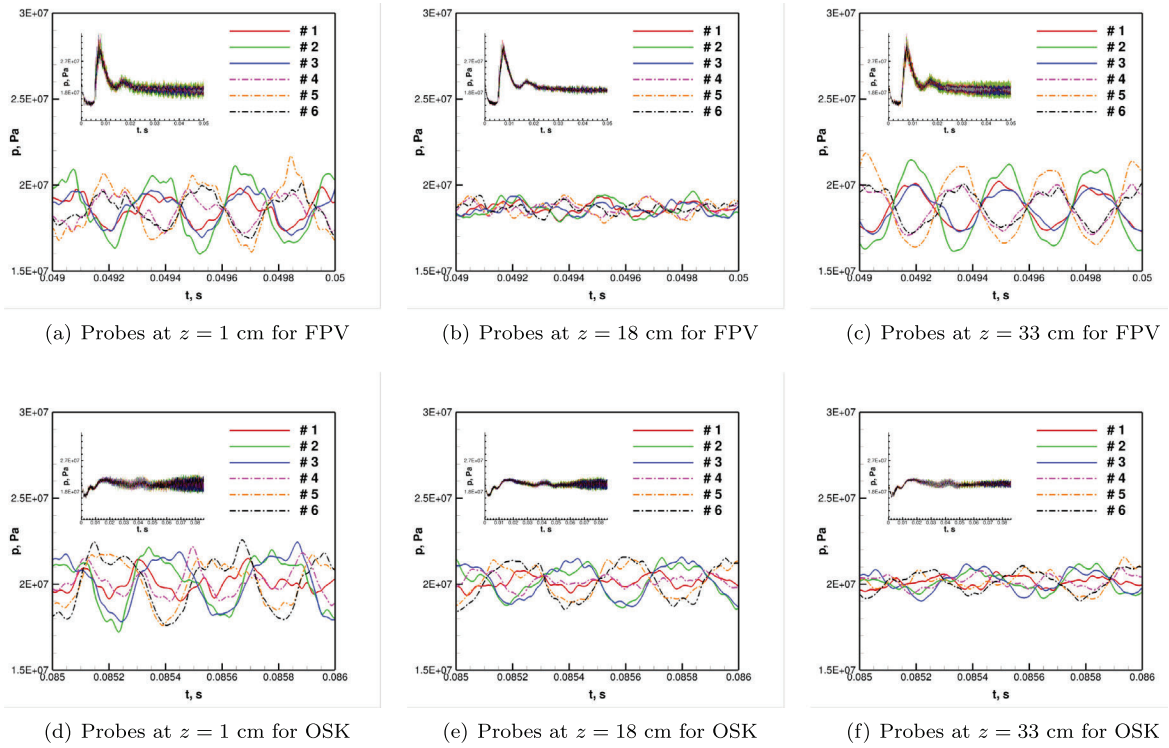

(a) Probes at $z = 1$ cm for FPV (b) Probes at $z = 18$ cm for FPV (c) Probes at $z = 33$ cm for FPV

(d) Probes at $z = 1$ cm for OSK (e) Probes at $z = 18$ cm for OSK (f) Probes at $z = 33$ cm for OSK

Fig. 12. Time history of pressure at the near-wall probes.

FPV model. For this reason, the mesh that has been validated with the previous work [11] is directly used in this paper for both the OSK and the FPV models. Fig. 11(b) also shows reactions take place in the downstream half of the chamber as well as in the nozzle for the FPV model. This feature plays a key role to distinguish the FPV simulation from the OSK simulation in terms of thermal-acoustic behavior.

3.3. Combustion instability analysis of the ten-injector liquid rocket engine

As shown in Fig. 8(a), the oscillatory temporal variation of the total mass flow rate at the nozzle outlet indicates combustion instability. To monitor the possible tangential behavior of the combustion instability, we record the time histories of pressure on six probes placed 1 mm away from the chamber wall and equally distributed in the circumferential direction as shown in Fig. 5(b). To facilitate the analysis of possible longitudinal instability, we put three groups of such probes at three different axial locations downstream from the injector plate, which are $z = 0.01$ m, $z = 0.18$ m and $z = 0.33$ m. Each subfigure of Fig. 12 shows pressure histories from time 0. It is clear that the pressure at all near-wall probes reaches limit-cycle oscillation (LCO) in the last ten milliseconds for both the FPV and OSK models.

The CPU time consumption during LCO is summarized in Table 1 for both the FPV and OSK models. We implemented the tests on a desktop with a 2.9 GHz Intel core i7 CPU and a memory of 64 GB. The test time interval is roughly one period of LCO for each combustion model. The FPV model allows smaller average time step than the OSK model although they both employ the same CFL number, indicating the run with the FPV model marches forward slower. However, the CPU time consumption per time step is much lower for the FPV model. Note that the same number of transport equations are solved for both models. Hence, the comparison on the CPU time per time step implies the table look-up process in the FPV model is faster than the chemistry solving process in the OSK model even though the chemical processes considered by FPV are far more detailed and complex. Based on the test results, the total CPU time spent within LCO of ten milliseconds can be reasonably estimated. We found the FPV model is even more affordable than the OSK model in the current combustion instability analysis and this evaluation justifies FPV model's advantage in numerical efficiency.

Zoom-in view of pressure time histories in the last 1 ms is also provided in Fig. 12. We can uncover the type of the dominant mode from it by comparing the oscillation amplitude and phase among different probes. For the FPV model, pressure oscillation achieves maximum amplitude near injection plate (z = 1 cm) and nozzle entrance (z = 33 cm) while remaining at noise level around mid-chamber (z = 18 cm). This indicates a longitudinal standing wave with pressure antinodes at both ends of the chamber and a pressure node in the middle. At both ends of the chamber, pressure fluctuations are in phase at one group of probes (1, 2 and 3). At the other group of probes (4, 5 and 6), pressure oscillations are in phase as well but 180-degree out of phase with those at the previous group of probes. This also suggests a tangential standing mode with pressure antinodes at probes 2 and 5 as maximum oscillation amplitude appears at those probes. Hence, the dominant instability mode for FPV is a mixed longitudinal and tangential standing wave mode. For OSK, the amplitude of pressure oscillation decreases in the main flow direction. On any chamber cross-section, pressure fluctuations at one group of probes (2 and 3) are in phase. At another group of probes (5 and 6), pressure oscillations are also in phase but 180-degree out of phase with those at the previous group of probes. These facts suggest a dominant pure tangential standing mode with pressure nodes at probes 1 and 4 as minimum oscillation amplitude occurs at those probes.

To identify the frequency of the sustained oscillation, 512 sampling points are placed during the last 10 ms of the pressure time history. The Power spectral density (PSD) analysis is directly performed over these 512 sampling points, leading to a frequency resolution of 100 Hz, which is the same as in Ref. [7–9]. Fig. 13 shows that the dominant frequency is 3200 Hz for the FPV simulation and 2600 Hz for the OSK simulation. Note that we just focus on the highest peak in the pressure PSD amplitude. The rest peaks are at least ten times lower and hence has much less impact on the acoustic instability. For this reason, no windowing is applied to reduce spectral leakage. The frequency of

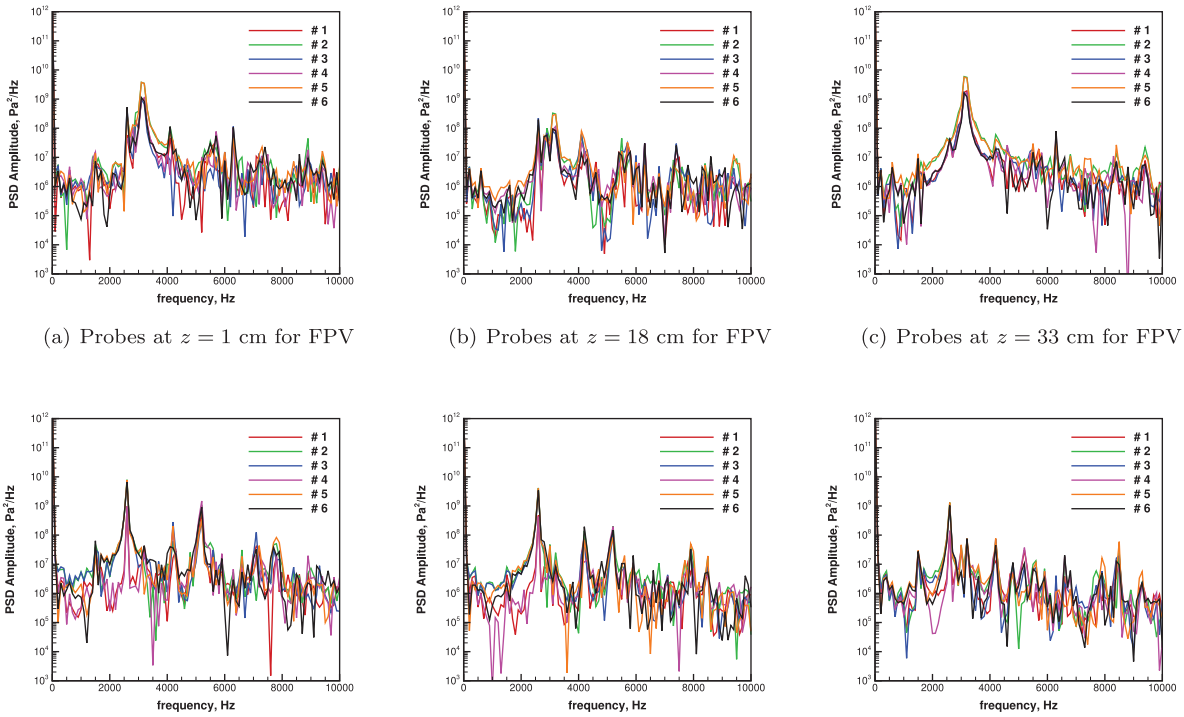

(a) Probes at $z = 1$ cm for FPV (b) Probes at $z = 18$ cm for FPV (c) Probes at $z = 33$ cm for FPV

(d) Probes at $z = 1$ cm for OSK (e) Probes at $z = 18$ cm for OSK (f) Probes at $z = 33$ cm for OSK

Fig. 13. PSD amplitude of pressure at the near-wall probes.

the dominant acoustic mode can be also estimated theoretically as summarized in the appendix. For the FPV model, the mean specific heat ratio $\bar{\gamma}$, the mean gas constant $\bar{R}$, the mean temperature $\bar{T}$ in the chamber are 1.20, 426.5 J/kg/K, and 2990.8 K. The mean speed of sound $\bar{c}$ in the chamber is 1229.77 m/s, leading to an estimated frequency of 3179.1 Hz for the first-order combined tangential and longitudinal mode. Although the OSK model predicts a much higher $\bar{T}$ of 4167.6 K, it yields lower $\bar{\gamma}$ and $\bar{R}$, which are 1.15, 323.8 J/kg/K. As a result, $\bar{c}$ for the OSK model is 1235.38 m/s, which is just a little higher than that for the FPV model and yields an estimated frequency of 2585.4 Hz for the first-order pure tangential mode. The computational results of the dominant frequency matches the theoretical estimation very well for both the FPV model and the OSK model. This indicates the resonant acoustic modes predicted by both models are physically allowed.

The wave pattern of the dominant instability mode can be clearly illustrated through the instantaneous contours of the pressure fluctuation produced by that mode. These instantaneous contours are obtained by rebuilding the pressure time history at each spatial point using only the identified dominant Fourier mode, which is the 3200 Hz mode for the FPV model and the 2600 Hz mode for the OSK model. As shown in Fig. 14, on the $z = 0$ cm cross-sectional plane a pair of pressure antinodes (opposite in signs) and a pair of nodes appear at fixed azimuthal positions for both the FPV and the OSK model, indicating the characteristic of tangential standing wave for both models. However, for the FPV model, the azimuthal orientation of the pressure antinodes pair overlaps the straight line connecting probes 2 and 5, which is a symmetry axis of the injector distribution. For the OSK model, the pair of pressure nodes (rather than pressure antinodes) occur near probes 1 and 4, which also align in a direction of the injector symmetry.

For the FPV model, pressure anti-nodes formed immediately downstream of the injector plate and at the entrance of the nozzle. A pressure node appears downstream of the injector plate by half of chamber length. These features in the axial direction of the chamber are illustrated in Fig. 15(a) 15(c) 15(e) 15(g) and suggest a longitudinal standing wave. Hence, the dominant instability mode predicted by the FPV model is a combined first-tangential and first-longitudinal standing wave mode. In contrast, the longitudinal-wave behavior is not observed for the OSK model. The pressure fluctuation monotonically decay in the main flow direction, suggesting that the OSK model favors a pure first tangential standing wave mode. Although the two combustion models differ in whether having turbulence/combustion sub-grid interaction, it seems that the thermal-acoustic behavior is more sensitive to the chemical kinetics detailedness and thus local heat release determined by it. Dramatic change in prediction of chamber temperature, concentration and reaction rate of major products is proof of this conclusion.

Using the Rayleigh index, we can determine the correlation between pressure fluctuation and unsteady heat release. In this paper, the Rayleigh index is calculated as:

$$RI = \frac{1}{\tau p_a} \int_{t_0}^{t_0+\tau} \frac{\gamma - 1}{\gamma} p' \omega'_T dt \tag{14}$$

where t_0 and τ are the lower limit and time interval which are determined such that the time integration is calculated over the last ten milliseconds for each model. p' is the local pressure oscillation, p_a is the local time-averaged pressure, γ is the specific heat ratio, and ω'_T is the local oscillation of heat release rate. Positive values (colored by red) of the Rayleigh index indicate pressure fluctuations are driven by the unsteady heat release, while negative values (colored by blue) suggest pressure oscillations are damped by the unsteady heat release.

Fig. 16 shows complicated pattern of mixed negative and positive Rayleigh index. This indicates the broad frequency band of the fluctuating pressure and heat release rate, which is typical in turbulent combustion. However, the driving mechanism to sustain the dominant instability mode can be identified by the fact how the regions of large positive Rayleigh index clusters. As shown by Urbano et al. [7], near the pressure antinodes of the dominant instability mode that are close to the injector plate, the reacting jet regions are colored by deep red, indicating pressure fluctuation is driven by unsteady heat release. At the same time, such driving mechanism is much weakened in the regions of two reacting jets near the pressure nodal line as

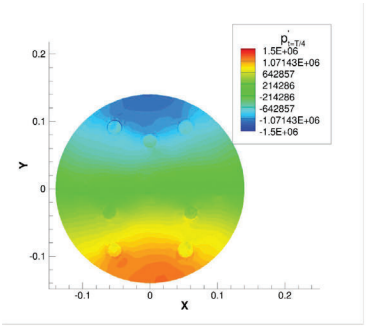

(a) 3200 Hz mode at $t = T/4$ for FPV

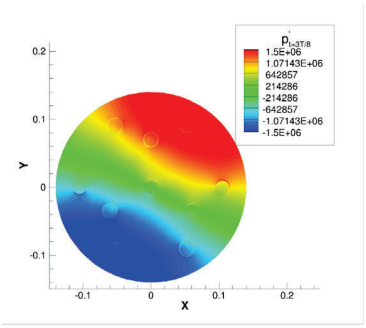

(b) 2600 Hz mode at $t = T/4$ for OSK

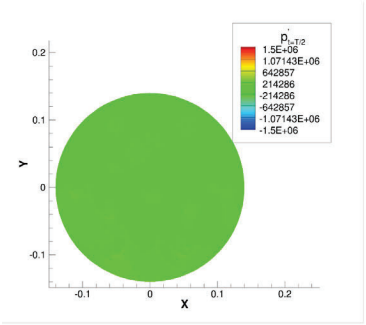

(c) 3200 Hz mode at $t = T/2$ for FPV

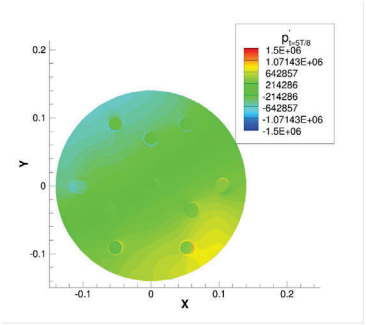

(d) 2600 Hz mode at $t = T/2$ for OSK

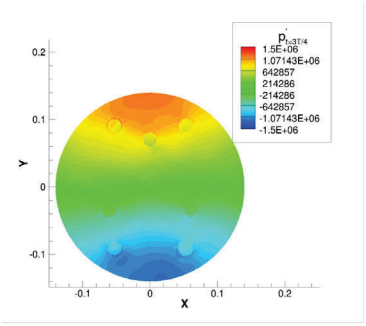

(e) 3200 Hz mode at $t = 3T/4$ for FPV

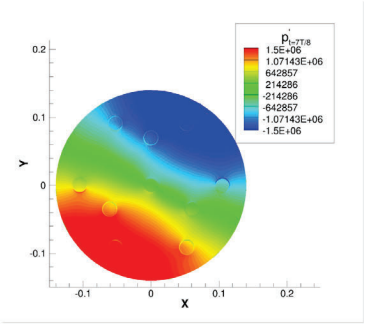

(f) 2600 Hz mode at $t = 3T/4$ for OSK

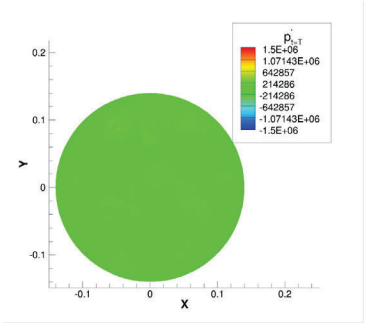

(g) 3200 Hz mode at $t = T$ for FPV

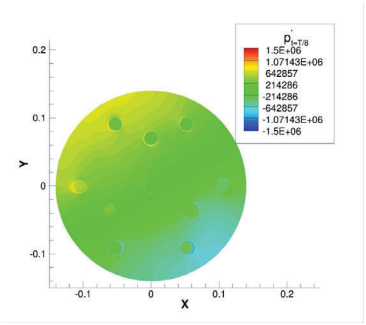

(h) 2600 Hz mode at $t = T$ for OSK

Fig. 14. Instantaneous contours of pressure fluctuation for the dominant instability mode on the z = 0 cm plane.

red color is rarely present. This is why the dominant instability mode has a tangential standing wave shape. For both the FPV and OSK simulations, the distribution of regions of large positive Rayleigh index (colored by deep red) shown in Fig. 16(c) and 16(d) is consistent with the azimuthal locations of the pressure nodes and anti-nodes of their dominant instability modes. As shown in Fig. 10, for both combustion models, the premixed flames are dominant in the immediate downstream of the injector plate where the fluctuation amplitudes of the pressure antinodes for the transverse acoustic standing wave reach maximum values (usually decay in the downstream axial direction). So, the interaction between the transverse acoustic standing wave and the premixed flames can be reasonably expected to be highly consequential. The two combustion models predict different mixing processes in the vicinity of the injector plate and hence distinct premixed flames including those stretched ones. This could be a major reason for the difference in the details of the predicted transverse wave by the two

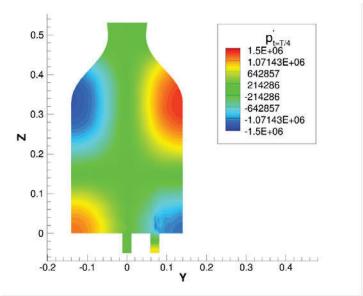

(a) 3200 Hz mode at $t = T/4$ for FPV

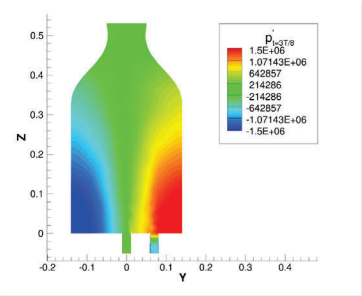

(b) 2600 Hz mode at $t = T/4$ for OSK

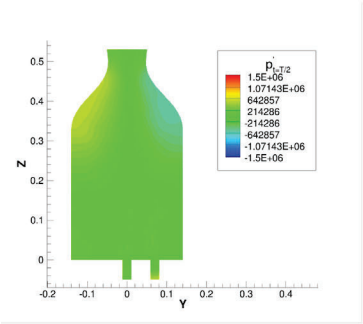

(c) 3200 Hz mode at $t = T/2$ for FPV

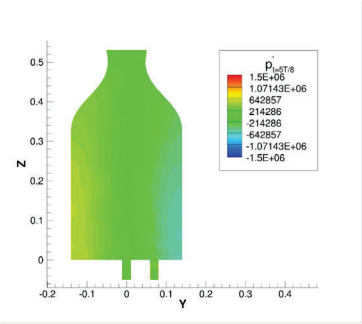

(d) 2600 Hz mode at $t = T/2$ for OSK

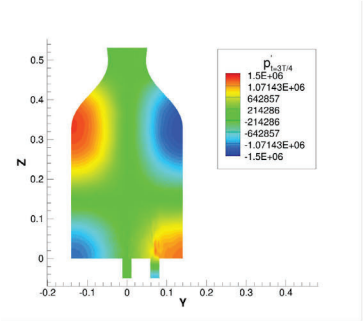

(e) 3200 Hz mode at $t = 3T/4$ for FPV

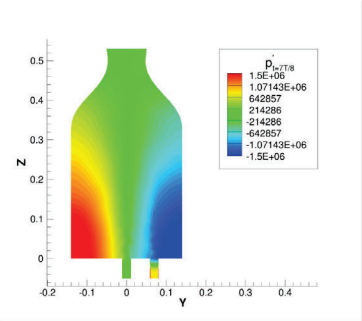

(f) 2600 Hz mode at $t = 3T/4$ for OSK

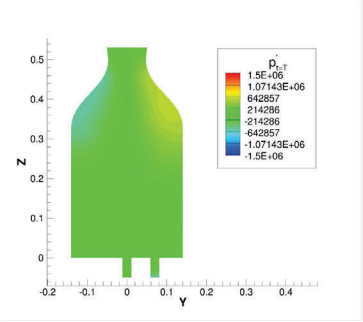

(g) 3200 Hz mode at $t = T$ for FPV

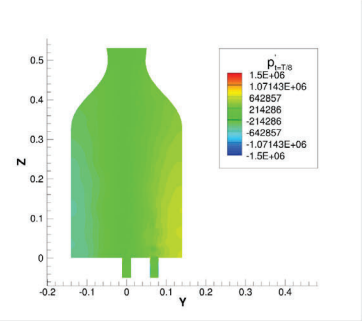

(h) 2600 Hz mode at $t = T$ for OSK

Fig. 15. Instantaneous contours of pressure fluctuation for the dominant instability mode on the $x = 0$ cm plane.

combustion models, such as the azimuthal locations of the pressure nodes/anti-nodes. Near the entrance of the exhaust nozzle, despite the leak of propellants, little reaction occurs in the OSK simulation. Pressure oscillation is at noise level as almost no heat is released there. For the FPV simulation, reactions among intermediate species take place near the nozzle entrance, thus releasing significant amount of heat. Regions of large positive (deep red) Rayleigh index are also clustered in that area as shown in Fig. 16(a), indicating a pressure anti-node of longitudinal standing wave. On the cross-section at the nozzle entrance, because the dominant instability mode in the FPV simulation also has a tangential standing wave shape, the regions of large positive (deep red) Rayleigh index agglomerate in the azimuthal direction near the pressure anti-nodes as shown in Fig. 16(g).

As vorticity plays an important role in mixing and hence has impacts on combustion instability, we also study the correlation between pressure fluctuation and the disturbance of helicity, which is the streamwise vorticity. For both combustion models, helicity fluctuation is only significant in the vicinity of the propellant jets. So, its impact on the

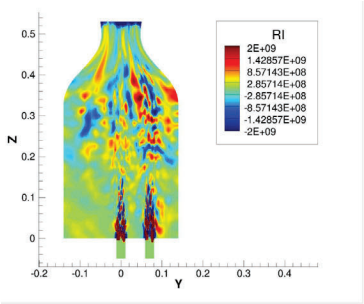

(a) $x = 0$ cm plane for FPV

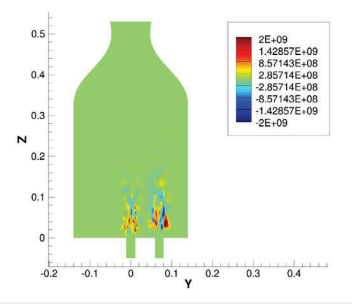

(b) $x = 0$ cm plane for OSK

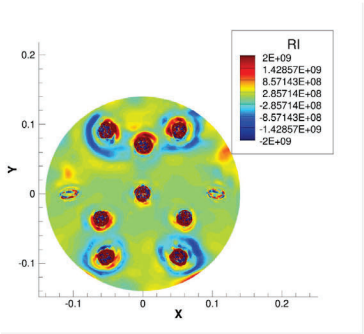

(c) $z = 4$ cm plane for FPV

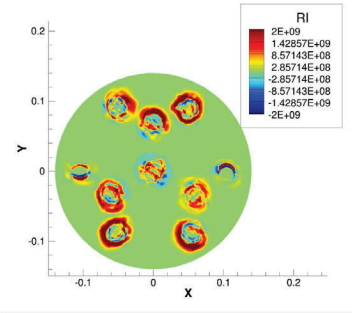

(d) $z = 4$ cm plane for OSK

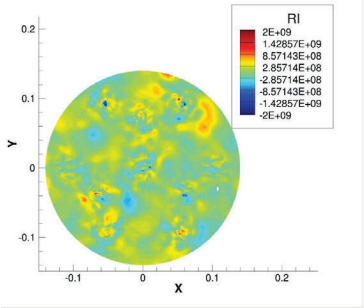

(e) $z = 15$ cm plane for FPV

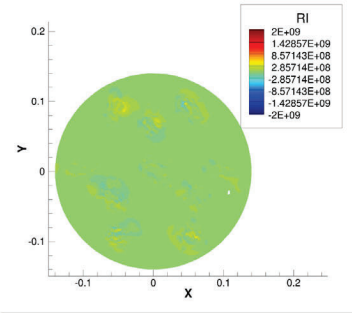

(f) $z = 15$ cm plane for OSK

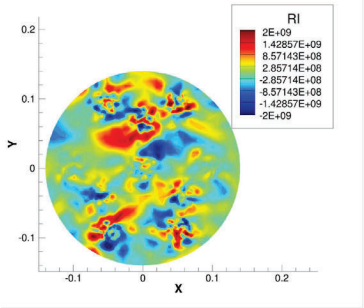

(g) $z = 33$ cm plane for FPV

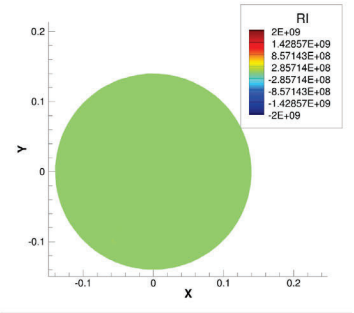

(h) $z = 33$ cm plane for OSK

Fig. 16. Contours of the Rayleigh index.

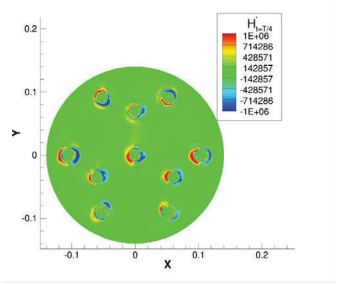

(a) Helicity mode at $t = T/4$

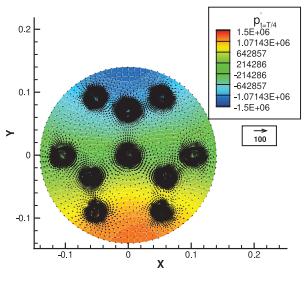

(b) Pressure and transverse velocity modes at $t = T/4$

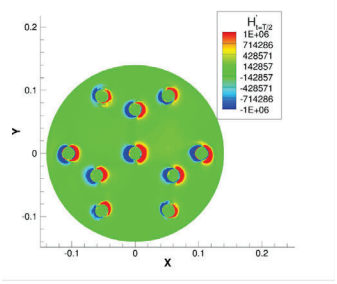

(c) Helicity mode at $t = T/2$

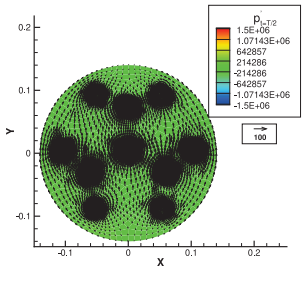

(d) Pressure and transverse velocity modes at $t = T/2$

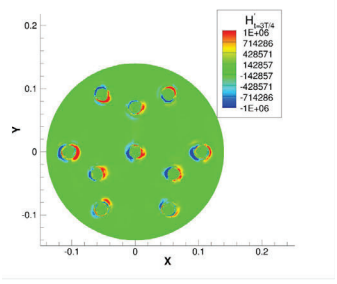

(e) Helicity mode at $t = 3T/4$

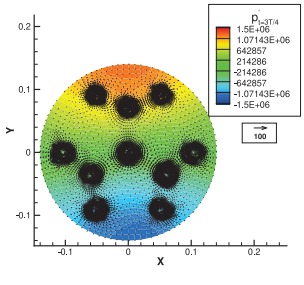

(f) Pressure and transverse velocity modes at $t = 3T/4$

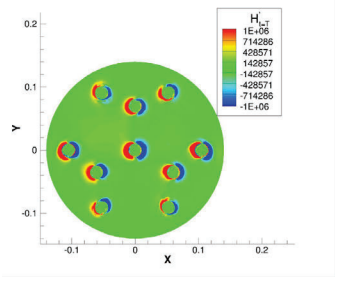

(g) Helicity mode at $t = T$

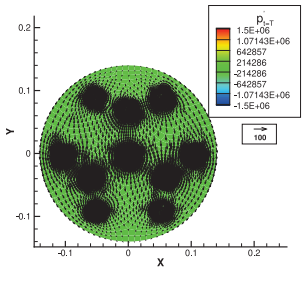

(h) Pressure and transverse velocity modes at $t = T$

Fig. 17. Correlation between pressure, transverse velocity and helicity fluctuation (3200 Hz) for FPV on the z = 1 cm plane.

flame dynamics and combustion instability is only important near the injector plate.

Plotting the contours on the $z = 1$ cm cross-sectional plane, we can correlate the pressure disturbance and the helicity fluctuation. Take the computation using the FPV model as an example, in Fig. 17, instantaneous helicity fluctuation is shown in the left column and the instantaneous pressure disturbance is shown in the right column at the same time instants. The maximum fluctuation in helicity appears when pressure fluctuation at the pressure anti-nodes is zero, indicating a phase difference of about 90 degrees between the pressure disturbance and the helicity fluctuation.

The helicity fluctuation is caused by the periodic transverse flow during a cycle of the dominant instability mode. Fig. 17 also shows the instantaneous projected velocity vector on the $z = 1$ cm cross-sectional

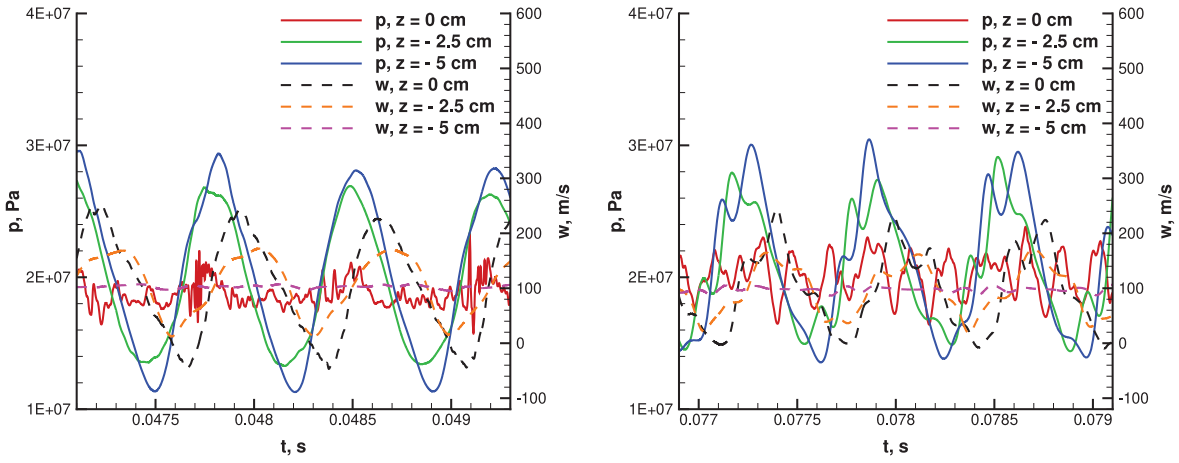

(a) FPV (b) OSK

Fig. 18. Time history of pressure and axial velocity inside the central oxidizer injector.

plane for the FPV model. At $T/4$, maximum pressure fluctuations occur at the pressure antinodes; however, the transverse velocity can be ignored in most of the cross-sectional plane. The upward pressure gradient drives an upward transverse flow which achieves the maximum speed $T/4$ later. At $T/2$, the pressure gradient vanishes and after this moment pressure gradient starts to establish again but in the downward direction. At $3T/4$, this pressure gradient reaches maximum, and the transverse flow stops temporarily. Later, the downward pressure gradient starts to trigger a downward transverse flow. The fastest downward transverse flow occurs at the end of the period T and at this moment the pressure gradient no longer exists. After this moment the transverse flow slows down and it finally leads to an upward pressure gradient. This process repeat periodically and it explains how the transverse standing mode is sustained. The similar coupling between pressure, helicity and transverse flow is also observed for the computation using the OSK model.

3.4. Resonance in the injectors

In this ten-injector analysis, the flow within the injector ports is simulated with a better resolution compared to that for configurations with a larger number of injectors [11–13]. Note that, inside the injectors, the current mesh resolution might still not be sufficient to adequately model turbulence and hence pressure loss. This may have some impact on the prediction of acoustic activity of the rocket engine. However, the discussion and refinement are beyond the scope of this paper.

The injector-plate face and injector exit are at $z = 0$ cm. The coordinate z inside the injector is negative. The injector port has a length of 5 cm with z varying from -5 cm to 0 cm within the port. Fig. 18(a) shows the oscillatory behavior in the central oxidizer port from an analysis using the FPV model. This resonance phenomenon is also found in other injectors but the oscillation magnitude can be different. The resonance inside injectors is believed to be triggered by the acoustic instability in the combustion chamber. Compared to the oxidizer injectors, the upstream domes and manifold feeding system seems to have little acoustic coupling with the combustion chamber when a transverse instability mode dominates in the chamber [7]. Since the dominant thermal-acoustic modes of the chamber have a transverse shape in the current testcase, ignoring it may not have significant influence on the acoustic activity of the rest engine components.

A pressure antinode (velocity node) occurs at $z = -5$ cm, the injector-port entrance, and a pressure node (velocity antinode) occurs at $z = 0$ cm, the injector exit. Note that, as shown in Fig. 15, the chamber dominant instability mode predicted by the FPV model is a combined first longitudinal and first tangential mode. Although a pressure antinode is identified near the injector plate for the longitudinal behavior, the pressure oscillation near the central injector exit is zero due to the tangential shape of the combined instability mode. This is consistent with the observation of acoustic oscillation inside the central injector that a pressure node is found at the injector exit. Further quantitative analysis finds, at $z = -2.5$ cm, the phase angle difference between pressure and the axial velocity is about 90 degrees, which can be also identified in Fig. 18(a). All these features suggest that the injector is behaving as a quarter-wave-length tube. Here, the exit of the injector behaves as an open end while the inlet behaves as a closed end. Although the injector inlet has mass flow, Fig. 18(a) shows that the axial velocity fluctuation there is almost zero. With this key feature, we identify the similarity between the injector inlet and a closed end when discussing the behavior of the acoustic waves inside the injector port. For pure oxygen at 400 K, the speed of sound is about 379 m/s. The theoretical frequency of this 5 cm quarter-wave-length resonance is 1895 Hz. The resonance frequency obtained in the computation is around 1400 Hz. The discrepancy with the theoretical estimation is due to the fact that the resonance conditions for a quarter-wave-length tube are not perfectly fulfilled at both ends of the injectors.

Similar oscillatory behavior occurs with the OSK model as shown in Fig. 18(b). Compared with the prediction of the FPV model, the resonance frequency remains almost unchanged as little reaction occurs inside the injector port with either model. However, the pressure oscillation magnitude at the injector inlet is smaller. The larger magnitude of pressure fluctuation at an off-set frequency in the combustion chamber predicted by the OSK model might have the effect of suppressing the resonance oscillation inside the injectors.

For the injector with the current length, its resonance has no impact on the main chamber oscillation as the frequency of the former deviates dramatically from that of the latter for both models. However, a shorter injector admits higher resonant frequency according to the quarter-wave-length tube theory. For a sufficiently short injector, the acoustic oscillation in the injector might affect the dominant chamber mode since the resonant frequency in the injector might overlap with that in the chamber. On the contrary, if the current injector becomes longer, the theoretically estimated resonant frequency in the injector deviates even more from the chamber resonant frequency, and hence the resonance in the injector is more unlikely to interfere with the dominant oscillation in the chamber. This situation could be modified if overtones appear with increasing length.

4. Conclusions

A compressible FPV model for methane and oxygen reaction at high pressure is developed and used to study the combustion instability for a ten-injector rocket engine. The governing equations for the FPV model are solved by a newly developed C++ code which is based on OpenFOAM 4.1. The Flamemaster code is used to generate the flamelet tables for methane/oxygen combustion at a background pressure of 200 bar. A 12-species kinetics is adopted to represent the chemical reactions. To address the pressure effect on the reaction rate for the progress variable while reducing computational effort in looking up the tables, the reaction rate is rescaled using a power law. The OSK model is also applied in computations as a comparison to the FPV model. In all computations, we utilize a DES turbulence model, a mesh with moderate resolution and a partial configuration for combustion simulation of the ten injector rocket engine where thermal-acoustic instability occurs. These choices are made to lower computational cost. Nevertheless, they are adequate for analysis of the dominant combustion instability behavior.

In this paper, the reference stoichiometric scalar dissipation rate at the quenching limit is extremely high due to the high background pressure, leading to very small characteristic diffusion time. However, the flame structures remain qualitatively similar to those at much lower background pressures. Compared with the OSK model, the FPV model predicts lower and more realistic mean temperature in the combustion chamber since much more detailed chemical kinetics is used. Although the fuel and oxidizer are not mixed until entering the combustion chamber, combustion using both combustion models is found partially premixed. The premixed flames dominate near the injector plate due to acoustics-enhanced mixing, while non-premixed flames of the leaked propellants prevail around mid-chamber. The contradiction with use of FPV is noted since it is based on a non-premixed model.

Fourier analysis of the computed time histories of pressure at the near-wall probes shows that a combined first longitudinal standing wave and first tangential standing wave mode of 3200 Hz is dominant for the FPV model while the OSK model favors a pure first tangential standing wave mode of 2600 Hz. The significant heat release in the downstream part of the combustion chamber drives the pressure fluctuation in the region and helps to establish the longitudinal oscillation behavior for the FPV model. Helicity also fluctuates at the dominant instability frequency for both models. However, its coupling with the flame dynamics and the combustion instability is only significant in the vicinity of the propellant jets. The helicity fluctuation is in phase with the unsteady transverse flow and is 90 degrees out of phase with the pressure oscillation.

Both the FPV and OSK models predict resonance phenomenon inside the injectors. Despite slight mismatch in the resonance frequency compared with the theoretical estimation, the injectors behave similar to quarter-wave-length tubes. The resonance inside injectors is believed to be induced by the acoustic instability in the combustion chamber. The resonance inside the injectors is weaker in the OSK prediction as it is suppressed by the larger magnitude of pressure fluctuation in the combustion chamber immediately downstream of the injector plate.

In the future, study of acoustic coupling among all parts of the rocket engine should also be considered by including the propellant dome and manifold in upstream of the injectors.

CRediT authorship contribution statement

Lei Zhan: Writing – original draft, Visualization, Validation, Software, Methodology, Investigation, Formal analysis, Data curation. **Tuan M. Nguyen:** Writing – review & editing, Software, Methodology, Formal analysis. **Juntao Xiong:** Writing – review & editing, Software, Resources. **Feng Liu:** Writing – review & editing, Supervision, Resources, Funding acquisition, Formal analysis. **William A. Sirignano:** Writing – review & editing, Supervision, Resources, Project administration, Funding acquisition, Formal analysis, Conceptualization.

Declaration of competing interest

The authors declare that they have no known competing financial interests or personal relationships that could have appeared to influence the work reported in this paper.

Acknowledgments

This research was supported by the U.S. Air Force Office of Scientific Research under grants FA9550-18-1-0392 and FA9550-22-1-0191, with Dr. Mitat Birkan as the program manager. Professor Heinz Pitsch of RWTH Aachen University is acknowledged for providing us access to the FlameMaster code. Professor Hai Wang of Stanford University is acknowledged for providing us with the FFCMy-12 chemical reaction mechanism for the methane/oxygen combustion.

Appendix A. Supplementary data

Supplementary material related to this article can be found online at https://doi.org/10.1016/j.combustflame.2024.113538.

References

[1] L. Crocco, S. Cheng, High-frequency combustion instability in rocket motors with concentrated combustion, J. Am. Rocket Soc. 23 (1953) 301–313.
[2] L. Crocco, S. Cheng, High-frequency combustion instability in rockets with distributted combustion, Symp. (Int.) Combust. 4 (1953) 865–880.
[3] L. Crocco, S. Cheng, Theory of combustion instability in liquid propellant rocket motors, in: AGARDograph No. 8, Butterworths, U.K, 1956.
[4] S. Gröning, D. Suslov, M. Oschwald, T. Sattelmayer, Stability behaviour of a cylindrical rocket engine combustion chamber operated with liquid hydrogen and liquid oxygen, in: 5th European Conference for Aerospace Sciences, 2013.
[5] S. Gröning, D. Suslov, J. Hardi, M. Oschwald, Influence of hydrogen temperature on the acoustics of a rocket engine combustion chamber operated with LOX/H2 at representative conditions, in: Proceedings of Space Propulsion, 2014.
[6] S. Gröning, J. Hardi, D. Suslov, M. Oschwald, Injector-driven combustion instabilities in a hydrogen/oxygen rocket combustor, J. Propul. Power 32 (2016) 560–573.
[7] A. Urbano, L. Selle, G. Staffelbach, B. Cuenot, T. Schmitt, S. Ducruix, S. Candel, Exploration of combustion instability triggering using large eddy simulation of a multiple injector liquid rocket engine, Combust. Flame 169 (2016) 129–140.
[8] A. Urbano, Q. Douasbin, L. Selle, G. Staffelbach, B. Cuenot, T. Schmitt, S. Ducruix, S. Candel, Study of flame response to transverse acoustic modes from the LES of a 42-injector rocket engine, Proc. Combust. Inst. 36 (2017) 2633–2639.
[9] W. Hwang, B. Sung, W. Han, K. Huh, B.J. Lee, H.S. Han, C.H. Sohn, J. Choi, Real-gas-flamelet-model-based numerical simulation and combustion instability analysis of a GH_2/LO_x rocket combustor with multiple injectors, Energies 14 (2021) 1–23.
[10] K. Guo, B. Xu, Y. Ren, Y. Tong, W. Nie, Analysis of tangential combustion instability modes in a LOX/Kerosene liquid rocket engine based on OpenFOAM, Front. Energy Res. 9 (2022) 1–10.
[11] J. Xiong, H. Morgan, J. Krieg, F. Liu, W.A. Sirignano, Nonlinear combustion instability in a multi-injector rocket engine, AIAA J. 58 (2020) 219–235.
[12] J. Xiong, F. Liu, W.A. Sirignano, Combustion dynamics simulation of a 30-injector rocket engine, Combust. Sci. Technol. 194 (2022) 1914–1942.
[13] J. Xiong, F. Liu, W.A. Sirignano, Combustion simulation of an 82-injector rocket engine, AIAA J. 60 (2022) 4601–4613.
[14] R.J. Jensen, H.C. Dodson, S.E. Claflin, LOX/Hydtocarbon combustion instability investigation, 1989, NASA-CR-182249.
[15] M.E. Harvazinski, W.E. Anderson, C.L. Merkle, Spontaneous analysis of self-excited combustion instabilities using two- and three-dimensional simulations, J. Propul. Power 29 (2013) 396–409.
[16] C.J. Morgan, K.J. Shipley, W.E. Anderson, Comparative evaluation between experiment and simulation for a transverse instability, J. Propul. Power 31 (2015) 1696–1706.
[17] M.E. Harvazinski, D.G. Talley, V. Sankaran, Application of detailed chemical kinetics to combustion instability modeling, in: 54th AIAA Aerospace Sciences Meeting, 2016.
[18] S. Srinivasan, R. Ranjan, S. Menon, Flame dynamics during combustion instability in a high-pressure, shear-coaxial injector combustor, Flow Turbul. Combust. 94 (2015) 237–262.

[19] R. Garby, L. Selle, T. Poinsot, Analysis of the impact of heat losses on an unstable model rocket-engine combustor using large-eddy simulation, in: 48th AIAA/ASME/SAE/ASEE Joint Propulsion Conference and Exhibit, 2012.
[20] S.V. Sardeshmukh, S.D. Heister, W.E. Anderson, Prediction of combustion instability with detailed chemical kinetics, in: 53rd AIAA Aerospace Sciences Meeting, 2015.
[21] M.E. Harvazinski, Modeling Self-Excited Combustion Instabilities using a Combination of Two and Three Dimensional Simulations (Ph.D. thesis), Purdue University, West Lafayette, Indiana, 2012.
[22] N. Peters, Laminar diffusion flamelet models in non-premixed turbulent combustion, Prog. Energy Combust. Sci. 10 (1984) 319–339.
[23] N. Peters, Turbulent Combustion, second ed., Cambridge University Press, Cambridge, U.K, 2000.
[24] T.M. Nguyen, P.P. Popov, W.A. Sirignano, Longitudinal combustion instability in a rocket engine with a single coaxial injector, J Propul Power 34 (2018) 354–373.
[25] R. Pecnik, V.E. Terrapon, F. Ham, G. Iaccarino, H. Pitsch, Reynolds-averaged Navier–Stokes simulations of the HyShot II scramjet, AIAA J. 50 (2012) 1717–1732.
[26] A. Saghafian, V.E. Terrapon, F. Ham, G. Iaccarino, H. Pitsch, An efficient flamelet-based combustion model for compressible flows, Combust. Flame 162 (2015) 652–667.
[27] C.D. Pierce, P. Moin, Progress-variable approach for large-eddy simulation of non-premixed turbulent combustion, J. Fluid Mech. 504 (2004) 73–97.
[28] N. Peters, B. Rogg, Reduced Kinetic Mechanism for Applications in Combustion System, in: Lecture Notes in Physics, Springer-Verlag, Berlin, New York, 1993.
[29] T.M. Nguyen, W.A. Sirignano, The impacts of three flamelet burning regimes in nonlinear combustion dynamics, Combust. Flame 195 (2018) 170–182.
[30] T.A. Pant, C. Huang, C. Han, S.V. Sardeshmukh, W.E. Anderson, H. Wang, Flamelet modeling studies of a continuously variable resonance combustor, in: 54th AIAA Aerospace Sciences Meeting, 2016.
[31] T.M. Nguyen, W.A. Sirignano, Spontaneous and triggered longitudinal combustion instability in a single-injector liquid rocket combustor, AIAA J. 57 (2019) 5351–5364.
[32] F.R. Menter, M. Kuntz, R. Langtry, Ten years of industrial experience with the SST turbulence model, in: 4th Internal Symposium on Turbulence, Heat and Mass Transfer, 2003, pp. 625–632.
[33] F. Menter, Two-equation eddy-viscosity turbulence models for engineering applications, AIAA J. 32 (1994) 1598–1605.
[34] M. Strelets, Detached eddy simulation of massively separated flows, in: 39th AIAA Aerospace Sciences Meeting, 2001.
[35] M. Ihme, C.M. Cha, H. Pitsch, Prediction of local extinction and re-ignition effects in non-premixed turbulent combustion using a flamelet/progress variable approach: 1. A priori study and presumed pdf closure, Combust. Flame 155 (2008) 70–89.
[36] M. Ihme, C.M. Cha, H. Pitsch, Prediction of local extinction and re-ignition effects in non-premixed turbulent combustion using a flamelet/progress variable approach: 2. Application in LES of sandia flames d and e, Combust. Flame 155 (2008) 90–107.
[37] Z. Shadram, T.M. Nguyen, A. Sideris, W.A. Sirignano, Neural network flame closure for a turbulent combustor with unsteady pressure, AIAA J. 59 (2021) 621–635.
[38] Z. Shadram, T.M. Nguyen, A. Sideris, W.A. Sirignano, Physics-aware neural network flame closure for combustion instability modeling in a single-injector engine, Combust. Flame 240 (2022) 111973.
[39] H. Pitsch, FlameMaster, A C++ computer program for 0D combustion and 1D laminar flame calculations, ver. V4.0.0, 2019, https://www.itv.rwth-aachen.de/en/downloads/flamemaster/. [Retrieved 7 2019].
[40] G.P. Smith, Y. Tao, H. Wang, Foundational fuel chemistry model version 1.0 (FFCM-1), 2016, https://web.stanford.edu/group/haiwanglab/FFCM1/pages/FFCM1.html.
[41] Y. Tao, G.P. Smith, H. Wang, Critical kinetic uncertainties in modeling hydrogen/carbon monoxide, methane, methanol, formaldehyde, and ethylene combustion, Combust. Flame 195 (2018) 18–29.
[42] H. Muller, F. Ferraro, F. Pfitzner, Implementation of a steady laminar flamelet model for non-premixed combustion in LES and RANS simulations, in: 8th International OpenFOAM Workshop, 2013.
[43] B.J. McBride, S. Gordon, M. Reno, Coefficients for calculating thermodynamic and transport properties of individual species, 1993, NASA-TM-4513.
[44] E. Knudsen, H. Pitsch, Capabilities and limitations of multi-regime flamelet combustion models, Combust. Flame 159 (2012) 242–264.
[45] K. Seshadri, N. Peters, Asymptotic structure and extinction of methane-air diffusion flames, Combust. Flame 73 (1988) 23–44.
[46] D.T. Harrje, F.H. Reardon, Liquid propellant rocket combustion instability, 1972, NASA-SP-194.
[47] W. Armbruster, J.S. Hardi, Y. Miene, D. Suslov, M. Oschwald, Damping device to reduce the risk of injection-coupled combustion instabilities in liquid propellant rocket engines, Acta Astronaut. 169 (2020) 170–179.
[48] Y.C. Yu, J.C. Sisco, S.Rosen, A. Madhav, W.E. Anderson, Spontaneous longitudinal combustion instability in a continuously variable resonance combustor, J. Propul. Power 28 (2012) 876–887.
[49] H.G. Price, Cooling of high-pressure rocket thrust chambers with liquid oxygen, J. Spacecraft 18 (1981) 338–343.
[50] H.G. Price, P.A. Masters, Liquid oxygen cooling of high pressure LOX/Hydrocarbon rocket thrust chambers, 1986, NASA-TM-88805.
[51] E.S. Armstrong, J.A. Schlumberger, Cooling of rocket thrust chambers with liquid oxygen, in: 26th AIAA/SAE/ASME/ASEE Joint Propulsion Conference, 1990.
[52] E.A. Roncace, Liquid oxygen cooling of hydrocarbon fueled rocket thrust chambers, J. Propuls. 7 (1991) 717–723.
[53] H. Kojima, L. Kamps, Y. Nobuhara, G. Gallo, H. Nagata, Regenerative cooling of graphite nozzles for throat erosion suppression, in: 2023 AIAA SciTech Forum, 2023.
[54] G. Gallo, L. Kamps, S. Hirai, C. Carmicino, H. Nagata, One-dimensional modelling of the nozzle cooling with cryogenic oxygen flowing through helical channels in a hybrid rocket, Acta Astronaut. 210 (2023) 176–196.
[55] B. Fiorina, O. Gicquel, L. Vervisch, S. Carpentier, N. Darabiha, Approximating the chemical structure of partially premixed and diffusion counterflow flames using FPI flamelet tabulation, Combust. Flame 140 (2005) 147–160.